INFECTIOUS DISEASES

Ly6C^{hi} monocytes balance regulatory and cytotoxic CD4 T cell responses to control virus-induced immunopathology

Copyright © 2022 The Authors, some rights reserved; exclusive licensee American Association for the Advancement of Science. No claim to original U.S. Government Works

Céline Maquet[1], Jérôme Baiwir[1], Pauline Loos[1], Lucia Rodriguez-Rodriguez[1], Justine Javaux[1], Rémy Sandor[1], Fabienne Perin[2], Padraic G. Fallon[3], Matthias Mack[4], Didier Cataldo[2], Laurent Gillet[1]*†, Bénédicte Machiels[1]*†

Gammaherpesviruses (γHVs) have coevolved with their host, leading to a remarkably high infection prevalence and establishment of latency. The lifelong persistence of γHVs in hosts appears to broadly shape host immunity, and we show here that pulmonary infection with Murid herpesvirus 4 (MuHV-4), a mouse γHV, drives the recruitment of Ly6C^{hi} monocytes (MOs) into the airway, thereby modulating the host immune response. The absence of Ly6C^{hi} MOs is associated with severe virus-induced immunopathology and the systemic release of inflammatory mediators. Mechanistically, MuHV-4–imprinted MOs recruit CD4 T cells to the airways and trigger immunosuppressive signaling pathways through the PD-L1/PD-1 axis, thereby dampening the deleterious activation of cytotoxic CD4 T cells. These results uncover a role for Ly6C^{hi} MOs in modulating CD4 T cell functions and reveal pathways that could be targeted therapeutically to reduce detrimental immunopathological responses associated with respiratory viral infections.

Downloaded from https://www.science.org at Universit Catholique de Louvain on November 04, 2026

INTRODUCTION

Microorganisms are major environmental factors that play fundamental roles in training and modulating the host immune responses (*1*). In particular, the cross-talk between microbes and immune cells at the mucosal surface is critical for establishing an appropriate immune landscape (*2*). Viruses frequently infect the respiratory tract, and outcomes can range from asymptomatic to fatal illness. Attributes associated with the virus itself, the external environment, and the host contribute to disease heterogeneity. Variability in innate immune responses is one of the main factors associated with diverse disease responses to respiratory viral infections (*3*). A better understanding of these innate pathophysiological mechanisms is critical to identifying targets for specific therapeutic intervention. Of the players in innate immunity, monocytes (MOs) display remarkable plasticity and heterogeneity and play important roles in pathogen killing, immunomodulation, or sustaining inflammation in a context-dependent manner (*4*, *5*). Understanding the balance between proinflammatory and immunomodulatory pathways triggered by MOs upon viral infections is therefore of major importance.

Among the most prevalent human viruses, Epstein-Barr virus (EBV) and Kaposi's sarcoma–associated herpesvirus (KSHV) are two gammaherpesviruses (γHVs) associated with lifelong persistence in immune cells (*6*). Through coevolution with their host, γHVs have established a reciprocal beneficial relationship and appear to broadly influence the function of the immune system (*7*). The vast majority of EBV and KSHV infections are associated with mild symptoms in immunocompetent individuals, but they can markedly alter immune responses against unrelated antigens (*8*). The manipulation of B cells and evasion of T cell responses by γHVs have been widely studied, but how these viruses interact with the innate arm of the immune response is still poorly defined (*9*). We have recently shown that Murid herpesvirus 4 (MuHV-4), a γHV that infects mice, can protect against allergic asthma by inducing the replacement of resident alveolar macrophages (AMs) by MOs primed to have regulatory properties (*10*). However, the function of these MOs in γHV life cycle is not well understood, nor are their potential contributions to host-γHV interactions.

Here, we show that pulmonary infection with MuHV-4 induces the early recruitment of Ly6C^{hi} MOs in the airways, which contributes to the fine control of the host immune response. MuHV-4–imprinted MOs form clusters with CD4 T cells in their vicinity and promote regulatory cross-talk through immune checkpoint proteins. These results reveal a role for Ly6C^{hi} MOs in shaping the function of effector CD4 T cells and identify a key pathway that could be targeted by therapeutic strategies to mitigate host hyperinflammation.

RESULTS

MO deficiency leads to a severe MuHV-4–associated disease without affecting virus-specific adaptive immunity

MuHV-4 respiratory infection triggers the massive recruitment of MOs into the alveolar space at early time points after infection (*10*). These MOs exhibit increased expression of stem cell antigen 1 (Sca-1) and major histocompatibility complex class II (MHCII), which is associated with the acquisition of a regulatory profile (*11*). Expression of Sca-1 and MHCII on MOs trafficking from the bone marrow (BM) to the airways peaked at day 8 after infection (fig. S1, A to D) and correlated with production of the canonical regulatory interleukin-10 (IL-10) upon lipopolysaccharide (LPS) stimulation (fig. S1, E and F), suggesting immunomodulatory functions. Upon inflammation, emigration of Ly6C^{hi} MOs from the BM requires signals mediated by chemokine receptor CCR2 (*12*). We explored the role of Ly6C^{hi}

[1]Laboratory of Immunology and Vaccinology, Faculty of Veterinary Medicine, FARAH, ULiège, Liège 4000, Belgium. [2]Laboratory of Biology of Tumor and Development, GIGA-Cancer ULiège and "Centre Hospitalier Universitaire de Liège (CHU)", Liège 4000, Belgium. [3]School of Medicine, Trinity Biomedical Sciences Institute, Trinity College Dublin, Dublin 2, Ireland. [4]Department of Nephrology, University Hospital Regensburg, Regensburg, Germany.
*Corresponding author. Email: bmachiels@uliege.be (B.M.); l.gillet@uliege.be (L.G.)
†These authors contributed equally to this work.

MOs in the regulation of γHV life cycle by comparing the course of MuHV-4 pulmonary infection between wild-type (WT) and CCR2-deficient ($CCR2^{-/-}$) C57BL/6 mice (Fig. 1A). As expected, WT mice had a massive increase of $CCR2^{+}$ $Ly6C^{hi}$ MOs in the blood and bronchoalveolar fluids (BALFs) during MuHV-4 infection (Fig. 1, B and C) and did not display any clinical symptoms or substantial weight loss (Fig. 1D). In contrast, the absence of $Ly6C^{hi}$ MOs was associated with severe disease as indicated by weight loss and a massive inflammatory infiltrate into the lung parenchyma upon infection (Fig. 1, D and E). Similarly, MuHV-4–infected BALB/c mice, treated with anti-CCR2 antibody [MC21 monoclonal antibody (mAb)] (*13*), displayed transient depletion of MOs and showed greater weight loss and a more severe clinical score than counterparts treated with isotype control mAb (fig. S2). To examine changes to the biophysical properties of the lung over the course of MuHV-4 infection in the absence of MOs, we mechanically ventilated WT or $CCR2^{-/-}$ mice via tracheostomy and performed forced oscillation tests. WT mice showed normal lung biomechanics at day 8 after infection, but $CCR2^{-/-}$ mice had markedly abnormal values for most parameters, such as an increased respiratory system resistance and elastance, reduced compliance, and increased tissue damping and tissue elasticity (Fig. 1F). Besides, an alteration of blood parameter was also present with the increased hematocrit level (Fig. 1G). Although weight loss is transient and the alveolar niche is efficiently reconstituted in a CCR2-independent manner (fig. S3), this does not discount the crucial role of MOs in controlling acute infection. To evaluate the overall impact of MO deficiency on the disease phenotype, we measured survival after infection of WT or $CCR2^{-/-}$ mice with high doses of MuHV-4. Although WT mice recovered rapidly from the infection, all $CCR2^{-/-}$ mice succumbed to the same infection within 8 days (Fig. 1, I and J), demonstrating the major importance of MOs in preventing lethal virus-induced disease.

MOs are described to exert direct antiviral functions and to restrict viral replication (*14*, *15*). However, WT or $CCR2^{-/-}$ infected mice presented similar viral loads in the lung at days 8 and 15 after infection (Fig. 1H), supporting the idea that MuHV-4–imprinted MOs are not essential for viral clearance but, instead, may regulate excessive inflammation. We verified the absence of earlier viral replication in MO-depleted mice using a luciferase-expressing MuHV-4 strain (MuHV-4-Luc) (*16*), in C57BL/6 albino WT mice, treated with MC21 mAb or control mAb (Fig. 1K). Although the depletion of MOs was associated with severe weight loss (Fig. 1L), we quantified comparable levels of light emission and observed similar MuHV-4 replication rates (Fig. 1, M and N). MOs are known to be involved in T cell priming in various infection models (*17*). However, the establishment of MuHV-4–specific adaptive responses was comparable in the presence or absence of MOs, as demonstrated by the similar frequency and number of lung MuHV-4–specific $CD8^{+}$ T cells and by the similar level of MuHV-4–specific immunoglobulin G (IgG), measured at days 8, 15, and 30 after infection (Fig. 1, O to R). Together, these data suggest a critical role for MuHV-4–recruited MOs in the regulation of deleterious innate immune responses rather than in the priming of virus-specific adaptive responses.

MuHV-4–imprinted MOs prevent the development of the cytokine storm response

Evaluation of changes in innate cells during MuHV-4 infection in WT and $CCR2^{-/-}$ mice allowed us to identify a massive accumulation of neutrophils in the BALF of $CCR2^{-/-}$ mice (Fig. 2, A to C). This accumulation of neutrophils correlated with higher production of proinflammatory cytokines including IL-6, interferon-γ (IFN-γ), and tumor necrosis factor–α (TNF-α) in BALF (Fig. 2D). Of note, IL-6, type I IFN, and granulocyte-macrophage colony-stimulating factor (GM-CSF) concentrations also increased during infection in the blood of $CCR2^{-/-}$ mice compared with WT mice (Fig. 2E), suggesting that the absence of MOs has broader consequences than local tissue production of cytokines. Neutrophils play multiple roles in acute viral infections and are detrimental in some viral respiratory diseases (*18*). To assess whether neutrophil accumulation in the airways contributed to the immunopathological responses to infection, we treated WT and $CCR2^{-/-}$ mice with anti-Ly6G–depleting antibodies from day 4 to day 8 after MuHV-4 infection (Fig. 2F). The systemic injection of anti-Ly6G antibodies led to efficient neutrophil depletion, but weight loss and BALF cytokine concentrations were comparable in the presence or absence of neutrophils for infected $CCR2^{-/-}$ mice (Fig. 2, G to J), indicating that recruited neutrophils are not the major drivers of the disease. Uncontrolled release of proinflammatory cytokines, commonly described as a "cytokine storm," has detrimental systemic consequences in several respiratory viral infections, including influenza (*19*) and coronavirus disease 2019 (COVID-19) (*20*). To assess whether a similar mechanism occurred in MuHV-4–infected mice in the absence of recruited MOs, we quantified the cytokine response in the BALF and blood of WT and MO-depleted mice over the course of infection (Fig. 2, K to N). Similar to $CCR2^{-/-}$ mice, MO depletion was accompanied by massive neutrophil infiltration in the BALF of MuHV-4–infected mice (Fig. 2L). Furthermore, we confirmed that the absence of MOs triggered a massive release of proinflammatory cytokines in the BALF and blood of MuHV-4–infected mice lacking MOs (Fig. 2, M and N). This experiment also showed a higher concentration of IL-10 in the BALF of MuHV-4–infected WT mice compared with MO-depleted mice. This observation suggested that recruited MOs may protect against virus-induced immunopathology through local production of regulatory cytokines.

MuHV-4–imprinted MOs drive the recruitment of IL-10–producing CD4 T cells in the airways

To determine whether IL-10 plays an essential role in the control of MuHV-4–associated pathology, we followed disease progression during infection in WT and IL-10–deficient ($IL\text{-}10^{-/-}$) mice (Fig. 3A). The absence of IL-10 led to a severe worsening of pathology as evidenced by higher weight loss (Fig. 3B), BALF neutrophilia (Fig. 3C), and a massive release of IFN-γ in both BALF and blood (Fig. 3D). To decipher whether IL-10 production by MOs is a key mechanism controlling disease severity, we generated an inducible conditional mutant mouse, $Ccr2\text{-}creER^{T2}$ $IL\text{-}10^{lox/lox}$, in which Cre recombinase requires the presence of tamoxifen for activity (Fig. 3E) (*21*). This targeted depletion (Fig. 3F) did not increase weight loss or lung neutrophilia compared with MuHV-4–infected WT mice (Fig. 3, G and H), thus demonstrating that IL-10 produced by MOs is not the direct driver of the protective phenotype. To rule out any anomalous results due to Cre excision efficiency, we confirmed these results using mixed chimeras (fig. S4). Mice reconstituted with a mix (50:50) of $CCR2^{-/-}$ and $IL\text{-}10^{-/-}$ BM cells, which are deficient of any circulating IL-10–producing MOs, did not display any weight loss upon MuHV-4 infection (fig. S4B). Hence, we assessed IL-10 expression upon MuHV-4 infection across all lung cell populations using IL-10-β-lactamase reporter ITIB mice (*22*). This unbiased

Downloaded from https://www.science.org at Universit Catholique de Louvain on November 04, 2026

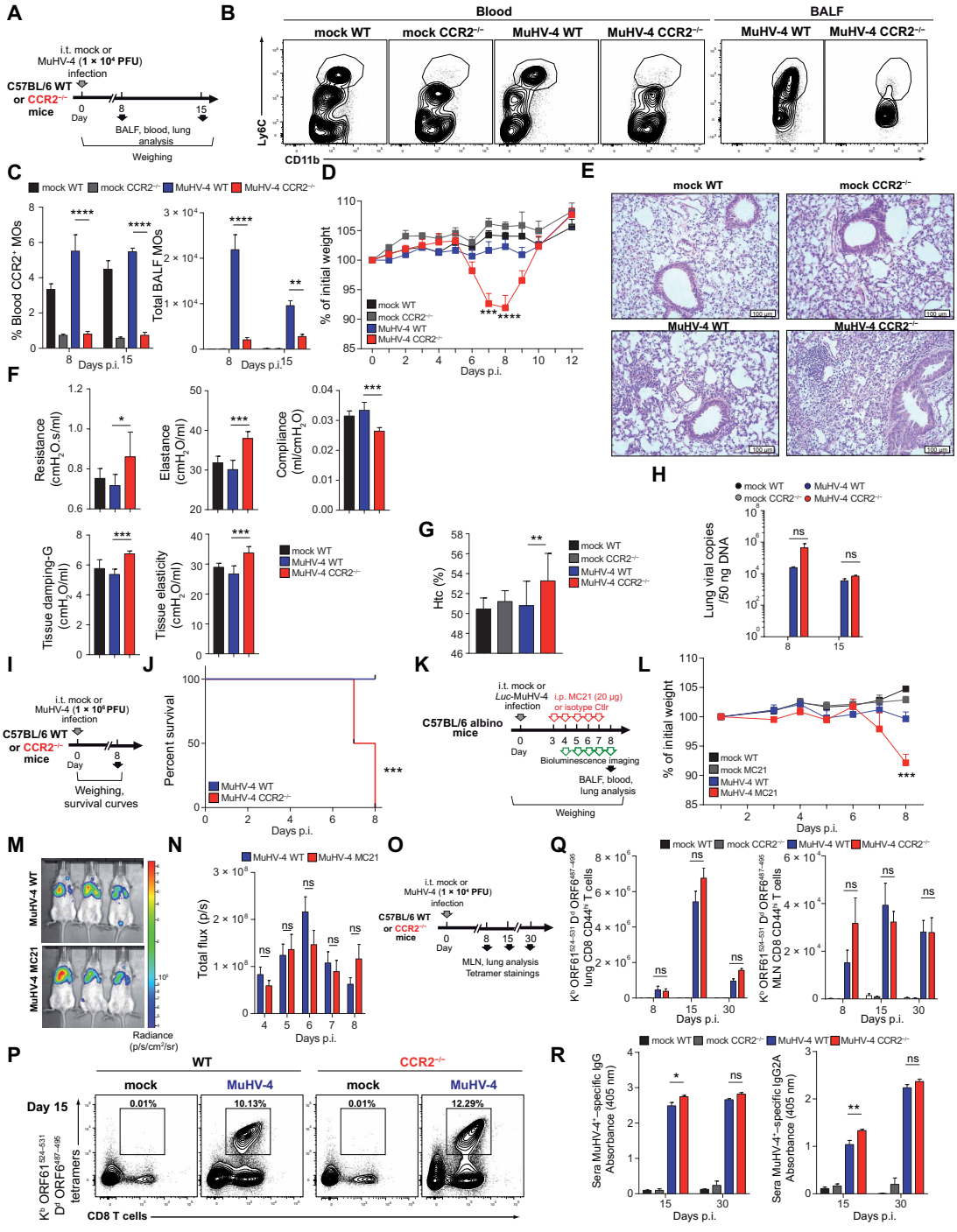


Fig. 1. MO deficiency leads to a severe MuHV-4–associated disease without affecting virus-specific adaptive immunity. (**A**) Experimental layout for (A) to (H). i.t., intratracheal. (**B**) Fluorescence-activated cell sorting (FACS) plots of Ly6C^{hi} MOs from blood and BALF (gated as described in fig. S1) at day 8 post-infection (p.i.). (**C**) Percentages and numbers of Ly6C^{hi} CCR2^{+} MOs in blood and BALF ($n = 4$ to 5, three experiments). (**D**) Body weight as percentage of initial weight ($n = 5$ to 10, three experiments). (**E**) Histological analysis of lung sections at day 8 after infection stained with H&E ($n = 4$, one experiment). (**F**) Respiratory mechanics parameters from the lung function assessment at day 8 after infection ($n = 4$ to 5, one experiment). (**G**) Hematocrit (Htc) measurement ($n = 5$ to 14, two pooled experiments). (**H**) MuHV-4 genome copies in lung ($n = 4$ to 5, three experiments). (**I**) Experimental layout for (I) and (J). (**J**) Survival curves ($n = 6$, one experiment). (**K**) Experimental layout for (K) to (N). (**L**) Body weight as percentage of initial weight ($n = 4$ to 6, two experiments). (**M**) Luciferase signals from infected mice at day 8 after infection ($n = 4$ to 6, two experiments). (**N**) Quantification of luciferase signals from infected mice ($n = 4$ to 6, two experiments). (**O**) Experimental layout for (P) to (R). (**P**) FACS plots of D^{b}ORF6$^{487–495}$ and K^{b}ORF61$^{524–531}$ MuHV-4–specific tetramer stainings of lung CD8 T cells. Numbers in gates indicate mean percentages of tetramer-positive cells in CD8^{+} T cells. (**Q**) Number of MuHV-4–specific tetramer^{+} CD8^{+} T cells in the lung and MLN ($n = 4$ to 10, three experiments). (**R**) Anti–MuHV-4 antibodies ($n = 2$ to 6, three experiments). For comparisons between multiple groups, one-way or two-way ANOVA was used with multiple-comparison tests. ns, not statistically different; *$P < 0.05$, **$P < 0.01$, ***$P < 0.001$, and ****$P < 0.0001$. Error bars represent SEM. See also figs. S1 to S3.

Downloaded from https://www.science.org at Universit Catholique de Louvain on November 04, 2026

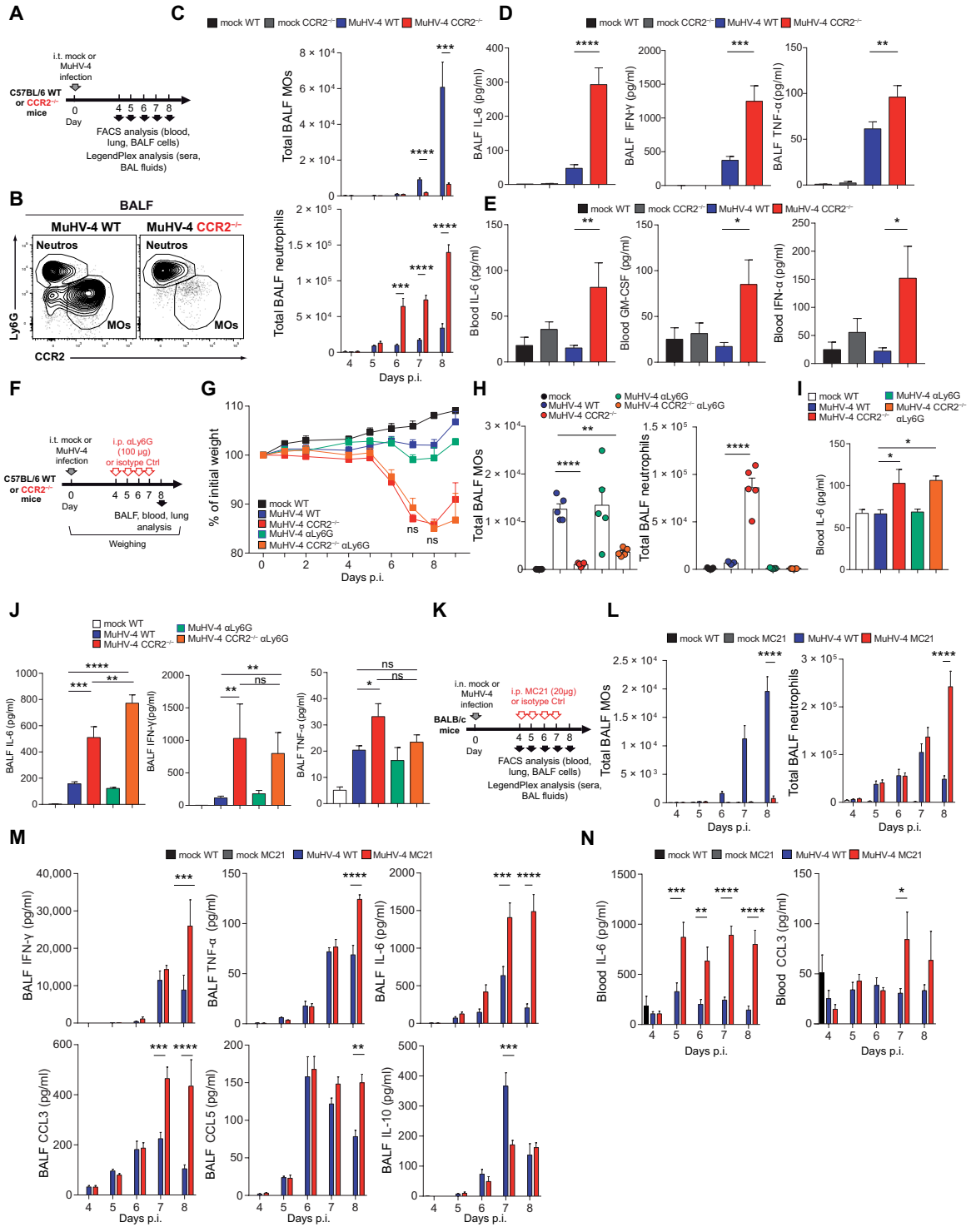


Fig. 2. MuHV-4–imprinted MOs prevent the development of the cytokine response. (**A**) Experimental layout for (A) to (E). (**B**) FACS plots of BALF MOs and neutrophils at day 8 after infection. (**C**) Numbers of BALF MOs and neutrophils ($n = 5$ to 6, three experiments). (**D** and **E**) Cytokine production in BALF (D) and sera (E) at day 8 after infection ($n = 4$ to 6, two experiments). (**F**) Experimental layout for (F) to (H). (**G**) Body weight as percentage of initial weight ($n = 6$ to 7, three experiments). (**H**) Numbers of neutrophils and MOs in BALF at day 8 after infection ($n = 5$, three experiments). (**I**) ELISA measurement of IL-6 in blood at day 8 after infection ($n = 4$ to 5, one experiment). (**J**) ELISA measurement of IL-6, IFN-γ, and TNF-α in BALF at day 8 after infection ($n = 4$ to 5, one experiment). (**K**) Experimental layout for (l) to (M). (**L**) Numbers of BALF MOs and neutrophils ($n = 2$ to 6, three experiments). (**M** and **N**) Cytokine production in BALF (L) and sera (M) from MC21-treated or untreated mock- or MuHV-4–infected mice ($n = 4$ to 6, one experiment). For comparisons between two groups, Student's two-tailed *t* test was used. For comparisons between multiple groups, one-way or two-way ANOVA was used with multiple-comparison tests. ns, not statistically different; $^*P < 0.05$, $^{**}P < 0.01$, $^{***}P < 0.001$, and $^{****}P < 0.0001$. Error bars represent SEM.

Downloaded from https://www.science.org at Universit Catholique de Louvain on November 04, 2026

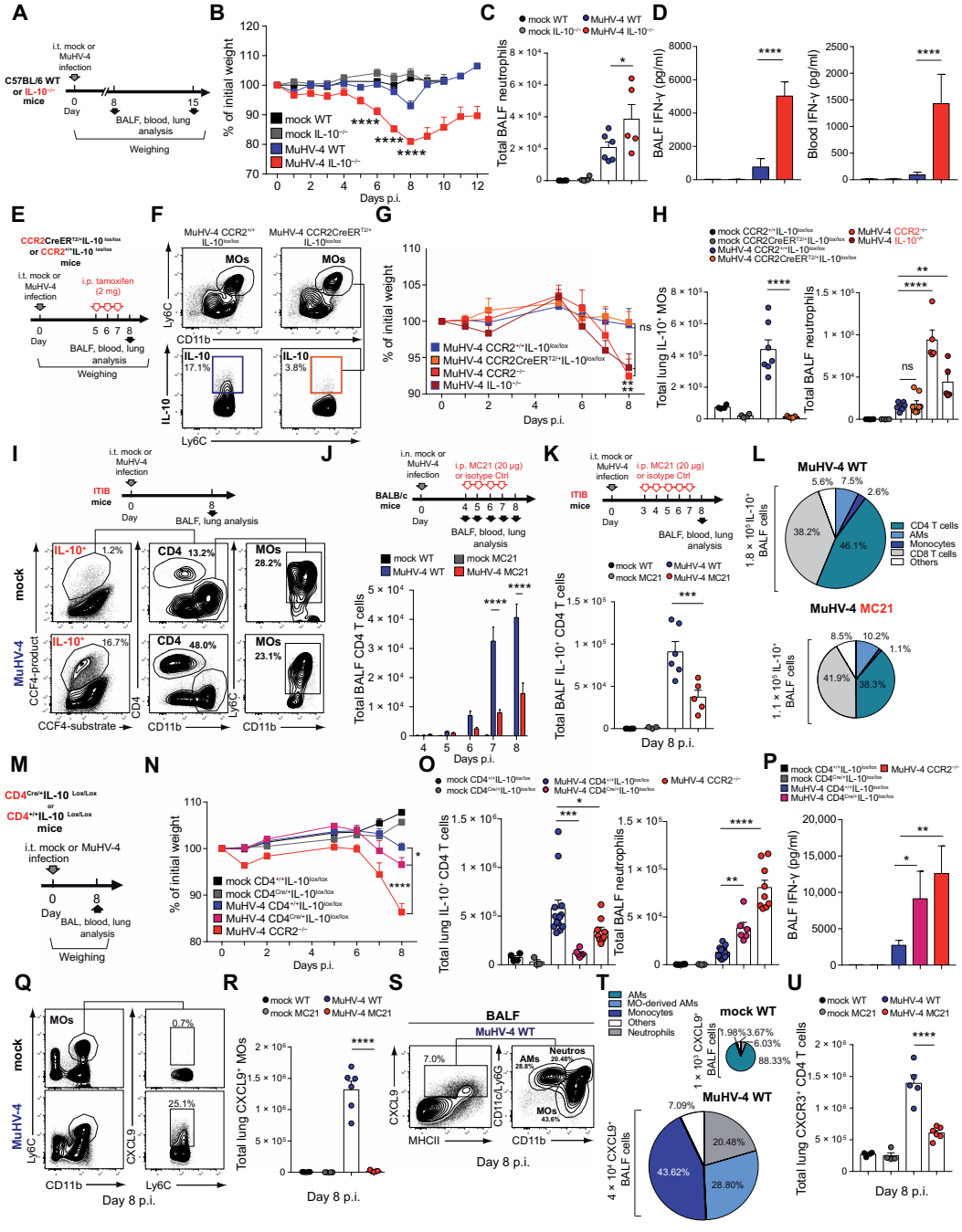


Fig. 3. MuHV-4–imprinted MOs drive the recruitment of IL-10–producing CD4 T cells in the airways. (**A**) Experimental layout for (A) to (D). (**B**) Body weight as percentage of initial weight ($n = 4$ to 14, three experiments). (**C**) Numbers of BALF neutrophils at day 8 after infection ($n = 4$ to 6, three experiments). (**D**) ELISA measurement of IFN-γ in BALF and blood at day 8 after infection ($n = 4$ to 6, one experiment). (**E**) Experimental layout for (F) to (H). i.p., intraperitoneal. (**F**) FACS plots of lung MOs expressing IL-10 after ex vivo stimulation with LPS. Mean percentages are shown. (**G**) Body weight as percentage of initial weight ($n = 5$ to 10, three experiments). (**H**) Numbers (day 8 after infection) of lung MOs expressing IL-10 after ex vivo stimulation with LPS and BALF neutrophils ($n = 4$ to 8, three experiments). (**I**) Experimental layout and FACS plots of IL-10 signals in CD4 T cells and MOs at day 8 after infection, assessed in lung cells from ITIB mice. Mean percentages are shown ($n = 4$ to 6, three experiments). (**J**) Experimental layout and numbers of BALF CD4 T cells ($n = 2$ to 6, three experiments). (**K**) Experimental layout for panels and numbers of BALF IL-10–expressing CD4 T cells ($n = 4$ to 6, three experiments). (**L**) Pie charts depicting the mean number and the proportion of the different IL-10$^+$ cells in BALF at day 8 after infection. (**M**) Experimental layout for (N) to (P). (**N**) Body weight as percentage of initial weight ($n = 4$ to 6, one experiment). (**O**) Numbers (day 8 after infection) of lung CD4 T cells expressing IL-10 after ex vivo stimulation with αCD3αCD28 purified antibodies and BALF neutrophils ($n = 3$ to 13, one experiment). (**P**) ELISA measurement of IFN-γ in BALF at day 8 after infection ($n = 3$ to 13, one experiment). (**Q** and **R**) FACS plots (Q) and numbers (R) of lung MOs expressing CXCL9. Numbers in gates indicate means ($n = 4$ to 6, three experiments). (**S**) FACS plots of CXCL9$^+$ BALF cells in MuHV-4–infected mice. Numbers in gates indicate means. (**T**) Pie charts depicting the mean number and the proportion of the different CXCL9$^+$ cells in BALF. (**U**) Numbers of lung CD4 T cells expressing CXCR3 ($n = 4$ to 6, one experiment). For comparisons between multiple groups, one-way or two-way ANOVA was used with multiple-comparison tests. ns, not statistically different; *$P < 0.05$, **$P < 0.01$, ***$P < 0.001$, and ****$P < 0.0001$. Error bars represent SEM. See also figs. S4 and S5.

Downloaded from https://www.science.org at Universit Catholique de Louvain on November 04, 2026

approach confirmed that MuHV-4 infection induced an increase of IL-10–producing cells in the airways and identified CD4 T cells as the main producers of IL-10 after MuHV-4 infection (Fig. 3I), raising the idea that MOs could play an essential regulatory role, affecting indirectly CD4 T cell function. On the basis of these findings, we monitored CD4 T cell infiltration in the BALF of MuHV-4–infected mice, treated with MC21-depleting antibody or control mAb. This experiment revealed that the absence of MOs correlated with marked impairment of CD4 T cell infiltration over the course of MuHV-4 infection (Fig. 3J). To more precisely determine whether MuHV-4–imprinted MOs affect the accumulation of IL-10–producing CD4 T cells in the lung, we treated ITIB mice with the MC21 or isotype control upon infection. The absence of MOs was associated with a strong reduction of IL-10–producing CD4 T cells in the airways (Fig. 3, K and L), suggesting that MuHV-4–imprinted MOs control disease severity by modulating the trafficking and functional properties of CD4 T cells.

Because MO-derived IL-10 appeared to be dispensable for direct control of viral pathology, we next assessed the relative importance of IL-10–producing T cells in maintaining homeostasis upon MuHV-4 infection by comparing the disease severity between CCR2$^{-/-}$ mice and conditional mutant mice CD4-cre IL-10$^{lox/lox}$ with respective littermates (Fig. 3M). The marked reduction of IL-10–producing CD4 T cells induced a partial phenotype characterized by weight loss, neutrophilia in the airways, and IFN-γ release that was intermediate between WT and CCR2$^{-/-}$ infected mice (Fig. 3, N to P). These results suggested that a defect in IL-10 production by CD4 T cells is critical but not sufficient to fully recapitulate the disease phenotype. A decrease in lung CD4 T cells in the absence of MOs could be the result of a defect in initial priming in the mediastinal lymph node (MLN) or a defect in lung tissue recruitment and local immune responses. Efficient priming of CD4 T cells was observed in both WT and CCR2$^{-/-}$ mice upon infection, as evidenced by similar numbers of CD4 T cells in the MLN (fig. S5, A and B) and equivalent proliferative capacities of these cells in the MLN and lung (fig. S5, C to F). Accordingly, we observed comparable activation and migratory capacities of conventional dendritic cells (cDCs) in WT and CCR2$^{-/-}$ mice upon infection. We detected negligible numbers of MO-derived DCs in the MLN (fig. S5, G and H), consistent with the low capacity of these DCs to migrate to LNs and prime T cell responses (*23*, *24*). We also assessed the ability of CD4 T cells to differentiate into regulatory T cells (T_{regs}) upon infection. This experiment revealed similar numbers of forkhead box P3–positive (FOXP3$^+$) MLN CD4 T cells in the infected groups and a reduced number of FOXP3$^+$ lung CD4 T cells in CCR2$^{-/-}$ mice (fig. S5, I and J). Therefore, these findings support the hypothesis that lung MOs may locally regulate the recruitment and activation of CD4 T cells rather than modulate initial priming or potential plasticity in the MLN.

During priming and activation, T cell trafficking into inflamed tissues is a dynamic process involving extravasation and chemotaxis via critical chemokines such as CXC ligand 9 (CXCL9), CXCL10, and CXCL11. In particular, CXCL9, whose expression is dependent on IFN-γ (*25*), interacts with the CXCR3 receptor and plays pleiotropic roles in migration, differentiation, and activation of CD8 and CD4 T cells (*26*, *27*). To address the importance of the CXCL9/CXCR3 axis in the control of MuHV-4–associated disease, we investigated CXCL9 production by lung leukocytes in WT and MO-depleted mice after infection. Our data revealed that MuHV-4–imprinted MOs from WT mice produce high concentrations of CXCL9 in the airways (Fig. 3, Q and R). In MuHV-4–infected WT mice, the main producers of CXCL9 were MOs and AMs, and these cells are mainly derived from MOs in MuHV-4–infected WT mice (Fig. 3, S and T) (*10*). In accordance with CXCL9 overproduction during infection, we observed a concomitant increase in CXCR3 expression on CD4 T cells (Fig. 3U), confirming the importance of the CXCL9/CXCR3 axis in bringing together MOs and MuHV-4–imprinted CD4 T cells in the airways. Overall, these data revealed a key role of MuHV-4–imprinted MOs in promoting local recruitment of CD4 T cells, including IL-10–producing CD4 T cells, and raised the hypothesis of potential cross-talk between these cell types to control the inflammatory response.

MuHV-4 infection promotes profound changes on both MO and CD4 T cell transcriptional programs

To assess the transcriptional diversity of MOs and CD4 T cells upon MuHV-4 infection, and to decipher potential transcriptomic alterations of CD4 T cells in the absence of MOs, both cell types were sorted from mock- or MuHV-4–infected WT or CCR2$^{-/-}$ mice at day 8 after infection and profiled by droplet-based single-cell RNA sequencing (scRNA-seq). To identify the potential functional heterogeneity between BALF and lung cells, hashtag oligomers were used as described (*28*) to multiplex cells across both sublocalizations (Fig. 4 and fig. S6, A and B). A total of 9682 cells (MOs and CD4 T cells from lung and BALF of mock- and MuHV-4–infected WT or CCR2$^{-/-}$ mice) were analyzed (fig. S6, C and D). We initially merged data from all samples, performed unsupervised clustering on highly variable genes, and projected cells in two dimensions using uniform manifold approximation and projection (UMAP) (Fig. 4B). This analysis confirmed the presence of two main populations corresponding to MOs and CD4 T cells. We then identified the origin of those cells based on respective hashtags.

Using an unsupervised clustering of single cells, we identified three and four major clusters of MOs and CD4 T cells, respectively (Fig. 4, C and F). Then, we selected the top 10 genes differentially expressed (DE) across clusters to define the phenotypic heterogeneity underlying each cell subcluster (Fig. 4, D and G). MO and CD4 T cell clusters differ largely in proportions and numbers upon infection. We observed enrichment of cluster 1 within the MO population and of clusters 0 and 2 within the CD4 T cells upon infection (Fig. 4, E and H). Analysis of DE genes on MOs and CD4 T cells identified 2511 DE genes in MOs and 2964 in CD4 T cells. Out of this list, the most relevant genes uniquely expressed between mock and MuHV-4 infection conditions were highlighted (Fig. 4, I and K) and selected for differential gene expression analysis within each specific cluster (Fig. 4, J and L).

Focusing on MOs, we observed that cluster 1 exhibited mixed features upon infection, characterized by a prominent chemokine secretory profile (e.g., *CCL8*, *CCL7*, *CCL2*, *CCL5*, *CXCL9*, *CXCL10*, and *CXCL16*), a regulatory signature (e.g., *Tgfbi*, *CD274*, *SPP1*, and *Ly6a*), an IFN-induced response (*Gbp2*, *Stat1*, *Isg15*, *Ifi47*, *Irf7*, *Oasl2*, and *Socs1*), and a typical antigen-presenting cell profile (e.g., *H2-Q7*, *H2-K1*, *H2-Ab1*, *H2-Aa*, and *CD74*) (Fig. 4J). In addition, BubbleGUM analysis (*29*) (Fig. 4M) confirmed strong enrichment upon infection in processes such as response to type I or type II IFN, antigen processing and presentation, regulation of leukocyte chemotaxis, regulation of T cell–mediated cytotoxicity, and T_{reg} differentiation. Feature plots of key transcripts involved in T cell chemotaxis and regulation, such as *CD274* [programmed cell death ligand 1 (PD-L1)],

Downloaded from https://www.science.org at Universit Catholique de Louvain on November 04, 2026

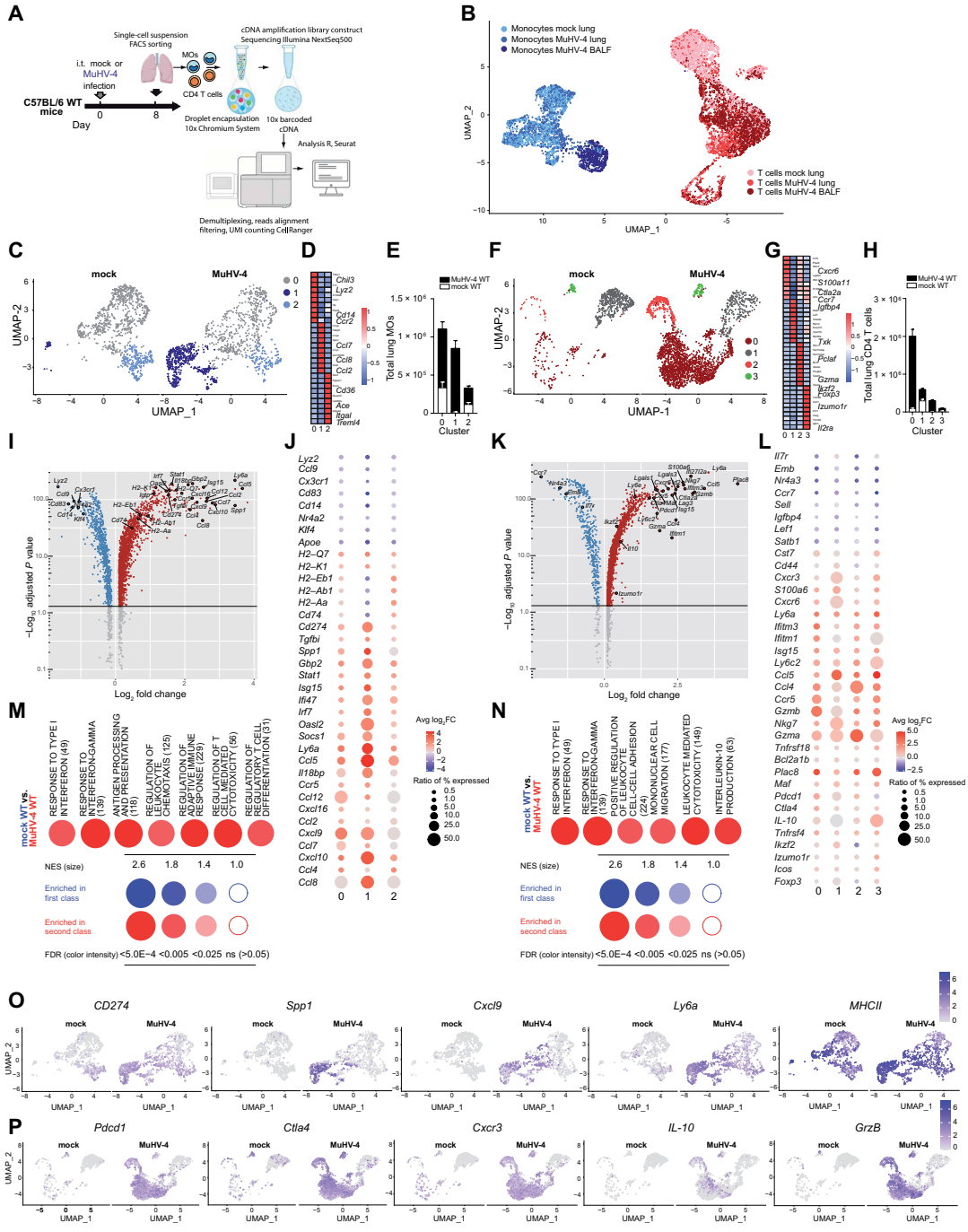


Fig. 4. MuHV-4 infection promotes profound changes on both MO and CD4 T cell transcriptional programs. (**A**) Experimental layout ($n = 4$ pooled mice by group, one experiment). (**B**) UMAP representation of scRNA-seq landscape. (**C**) UMAP representation of the top 20 PCs of MOs from mock- and MuHV-4–infected mice. (**D**) Heatmap of the 10 most DE genes for each cluster of MOs identified in (C). (**E**) Numbers of lung MOs per cluster and per condition. (**F**) UMAP representation of the top 20 PCs of CD4 T cells from mock- and MuHV-4–infected mice. (**G**) Heatmap of the 10 most DE genes for each cluster of CD4 T cells identified in (F). (**H**) Numbers of lung CD4 T cells per cluster and per condition. (**I**) Volcano plot of genes expressed by MOs of mock (blue)– and MuHV-4 (red)–infected mice. Light gray dots under the line represent nonsignificant genes (FDR < 0.05). (**J**) Dot plot of DE genes (*y* axis) by MO clusters (*x* axis). Dot size represents the ratio (MuHV-4/mock) of the number of cells in the cluster that express the gene, and color indicates the $\log_2$ fold change of the mean expression of each gene for a cluster. (**K**) Volcano plot of genes expressed by CD4 T cells of mock (blue)– and MuHV-4 (red)–infected mice. Light gray dots under the line represent nonsignificant genes (FDR < 0.05). (**L**) Dot plot of DE genes (*y* axis) by CD4 T cell clusters (*x* axis). Dot size represents the ratio (MuHV-4/mock) of the number of cells in the cluster that express the gene, and color indicates the $\log_2$ fold change of the mean expression of each gene for a cluster. (**M**) BubbleGUM analysis of seven Gene Ontology pathways from MOs of mock- and MuHV-4–infected mice. The number of genes considered in each pathway is indicated in parentheses. The color indicates the cell subset showing enrichment for the gene set. The color intensity indicates FDR. The surface area of the dots is proportional to the absolute value of the normalized enrichment score (NES). (**N**) BubbleGUM analysis of six Gene Ontology pathways from CD4 T cells of mock- and MuHV-4–infected mice. (**O**) UMAP representation of gene expression in MOs. (**P**) UMAP representation of gene expression in CD4 T cells. See also figs. S6 and S7.

Downloaded from https://www.science.org at Universit Catholique de Louvain on November 04, 2026

SPP1, or *MHCII*, showed similar distribution, mainly within cluster 1, suggesting functional importance of this specific MO subset to regulate T cell function (Fig. 4O).

A parallel approach was conducted on CD4 T cells (Fig. 4, K and L). Upon infection, cluster-specific analysis showed relatively reduced numbers of resting cells (expressing *Ccr7*, *Nr4a3*, *Emb*, *Il7r*, *Lef1*, and *Sell*), enrichment of activated cells displaying canonical tissue-resident memory/tissue effector memory markers [such as *CD44* and *Cxcr6* (*30*)], and enrichment of the T_{reg} populations (expressing *Foxp3*, *Icos*, *Izumo1r*, *Ikzfr*, *Tnfrsf4*, and *IL-10*). We also observed strong enrichment of activated cells with up-regulated expression of genes associated with IFN responses (*Ly6a*, *Ifitm3*, *Ifitm1*, *Isg15*, and *Ly6c2*), chemotaxis (*Ccl5* and *Ccl4*), cytotoxicity (*GrzB*, *GrzA*, and *Nkg7*), and costimulation or inhibition [*Pdcd1*, *Icos*, *Ctla4*, *Lag3*, *Tnfrsf18*, *c-Maf* (*31*), and *Plac8* (*32*)] (Fig. 4, K and L). Accordingly, BubbleGUM pathway analysis (Fig. 4N) confirmed general up-regulation of genes involved in IFN response, MO migration, cell-cell adhesion, leukocyte-mediated cytotoxicity, and IL-10 production. CD4 T cells exhibiting cytotoxic properties were initially identified in various viral infections (*33*, *34*), including MuHV-4 (*35*). Feature plots of highly DE genes revealed cosegregation of cells expressing *GrzB* with those expressing checkpoint mediators such as *Pdcd1* and *Ctla4* (Fig. 4P), suggesting that cytotoxic properties of CD4 T cell subsets could be strictly regulated during MuHV-4 acute infection in WT mice. Furthermore, concomitant expression of chemokines, such as *Cxcl9* and its receptor, *Cxcr3*, argues for key interactions between MuHV-4–imprinted MOs and activated CD4 T cells. NicheNet analysis (*36*) further supported this hypothesis by highlighting numerous ligand-target links between CD4 T cells and MOs involved in chemotaxis, intercellular adhesion, immune regulation, and inhibitory checkpoints (fig. S7, A and B), strengthening the existence of an important regulatory cross-talk between MuHV-4–imprinted MOs and CD4 T cells. Last, to determine any preferential sublocalization of MO and/or CD4 T cell subsets upon infection, we exploited hashtag identification of cells to analyze DE genes between BALF and lung compartments. Typical genes of MO cluster 1 were enriched in the BALF, indicating that MuHV-4–imprinted MOs mainly infiltrate the alveoli during infection. Similarly, activated CD4 T cells, exhibiting cytotoxic properties, were also enriched in the airways (fig. S7, C and D), demonstrating that these two populations of interest are located at the same place and are therefore likely to interact.

The absence of MuHV-4–imprinted MOs switches pre-armed cytotoxic CD4 T cells toward deleterious cell killers associated with severe tissue damages

We analyzed scRNA-seq data from MuHV-4–infected WT and $CCR2^{-/-}$ mice to dissect potential transcriptional alterations in CD4 T cells in the absence of regulation by MOs (Fig. 5A). This analysis revealed 355 CD4 T cell DE genes between WT and $CCR2^{-/-}$ MuHV-4–infected mice and highlighted the immunological dysregulation of CD4 T cells in the absence of MOs. We observed marked up-regulation of genes involved in cytotoxicity, such as *GrzA*, *GrzB*, *Nkg7*, *Prf1*, *GrzK*, *Ccl5*, *Runx3*, and *IFNγ* (Fig. 5B). BubbleGUM pathway analysis not only confirmed the enrichment in genes linked with cytotoxicity but also highlighted up-regulation of genes associated with cytokinesis, Golgi vesicle transport, and vesicle budding (Fig. 5C), suggesting not only exacerbated cytotoxicity but also enhanced secretion and degranulation of CD4 T cells from infected $CCR2^{-/-}$ mice. We evaluated the shift of CD4 T cells toward a cytotoxic phenotype in the absence of MOs during MuHV-4 infection by flow cytometry. This analysis revealed higher percentages of granzyme A (GrzA), granzyme B (GrzB), and CD107a (Fig. 5, D to F), confirming that CD4 T cells isolated from infected $CCR2^{-/-}$ mice exhibit stronger cytotoxic and degranulation activities than their counterparts isolated from WT infected mice. In line with these findings, higher amounts of GrzB were detected in BALF by enzyme-linked immunosorbent assay (ELISA) (Fig. 5G) and surface immunostainings (Fig. 5H). Moreover, although CD8 T cells and natural killer cells are the archetypal cytotoxic actors, we observed a large proportion of cells coexpressing CD4 and GrzB. Immunostaining of lung tissue revealed putative clusters of MOs and CD4 T cells in WT infected mice and highlighted the stronger cytotoxic and hyperinflammatory features of CD4 T cells in $CCR2^{-/-}$ mice. The difference in GrzB staining between WT and $CCR2^{-/-}$ infected mice was much higher with respect to extracellular GrzB release (Fig. 5I) than that observed by intracellular immunostaining (fig. S8, A and B), confirming that pre-armed cytotoxic CD4 T cells are more prone to degranulate in the absence of MOs.

Cytotoxic CD4 T cells have been shown to play important roles in both mice and humans in antiviral (*34*, *37*, *38*) and antitumoral immunity (*39*, *40*), as well as in response to vaccination (*41*). Although beneficial in many situations, they can also drive pathogenic immune responses and trigger tissue damages in an MHCII-restricted fashion (*42*–*44*). Epithelial and endothelial cells are known to overexpress MHCII molecules in an IFN-γ–dependent manner (*45*, *46*). Hence, in accordance with the high levels of IFN-γ released in the airways during MuHV-4 acute infection, we measured up-regulation of MHCII molecules on both epithelial and endothelial cells of WT and $CCR2^{-/-}$ MuHV-4–infected mice (Fig. 5J). Immunostaining of lung tissue from $CCR2^{-/-}$ mice revealed colocalization of GrzB-secreting CD4 T cells in close proximity to MHCII-positive endothelial and epithelial cells, whereas such clusters were more rarely found in MuHV-4 WT infected mice (Fig. 5, K and L, and fig. S8C). In line with these observations, we aimed at comparing tissue lesions and blood vessel damages. To this end, we first injected mice intravenously with tetramethylrhodamine (TRITC)–dextran to assess lung vascular permeability. Imaging of lung sections demonstrated larger diffusion of the fluorescent dye in the areas surrounding the blood vessels in $CCR2^{-/-}$ MuHV-4–infected mice, relative to their WT counterparts (Fig. 5, M and N). This increased vascular permeability measured in $CCR2^{-/-}$ MuHV-4–infected mice was further validated in MO-depleted mice by Evans blue quantification (*47*) in BALF and lung tissues after intravenous injection (Fig. 5O). Collectively, these data indicate that MuHV-4–imprinted MOs control the cytotoxic potential of recruited CD4 T cells and prevent them from mediating the detrimental killing of MHCII-expressing cells.

The PD-L1/PD-1 axis is crucial for the control of the cytotoxic features of CD4 T cells and for the maintenance of peripheral immune homeostasis

Transcriptional profiling of MOs and CD4 T cells after infection revealed potential key regulatory ligand-receptor pairs involved in the fine control of MuHV-4 acute inflammation (Fig. 4 and fig. S6). Among them, the PD-L1 (encoded by *CD274* gene)/PD-1 (encoded by *Pdcd1* gene) axis is known to play a fundamental role in evasion of immune defenses by tumor cells or chronic viral infections (*48*, *49*). The priming of MuHV-4–specific T cells is similar in the

Downloaded from https://www.science.org at Universit Catholique de Louvain on November 04, 2026

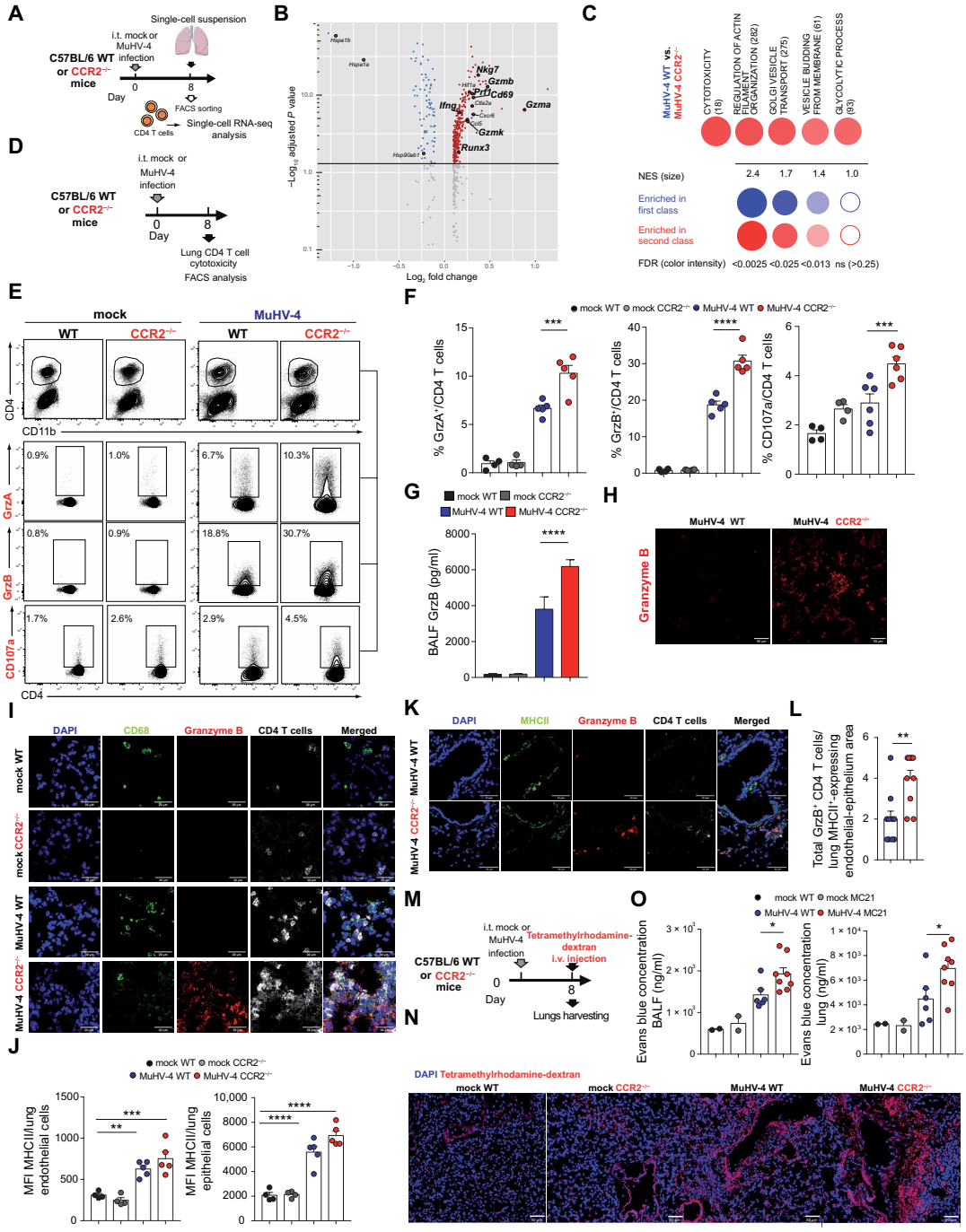


Fig. 5. The absence of MuHV-4–imprinted MOs switches pre-armed cytotoxic CD4 T cells toward deleterious cell killers associated with severe tissue damages. (**A**) Experimental layout for (A) to (C). (**B**) Volcano plot of genes expressed by CD4 T cells of MuHV-4 WT (blue) and MuHV-4 CCR2$^{-/-}$ (red) infected mice. Light gray dots under the line represent nonsignificant genes (FDR < 0.05). (**C**) BubbleGUM analysis of five Gene Ontology pathways from CD4 T cells from MuHV-4 WT and CCR2$^{-/-}$ mice. (**D**) Experimental layout for (D) to (L). (**E** and **F**) FACS plots (E) and percentages (F) of lung CD4 T cells expressing GrzA, GrzB, and CD107a at day 8 after infection. Numbers in gates indicate means ($n = 4$ to 6, three experiments). (**G**) ELISA measurements of GrzB and IFN-γ in BALF at day 8 after infection ($n = 4$ to 7, three experiments). (**H** and **I**) Low (H) and high (I) magnification of confocal microscopy images of lung sections stained for extracellular antigens. (**J**) Mean fluorescence intensity (MFI) of MHCII expression by endothelial cells and epithelial cells at day 8 after infection ($n = 4$ to 5, two experiments). (**K**) Confocal microscopy images of lung sections after immunofluorescent staining at day 8 after infection. (**L**) Quantification of GrzB^{+} CD4 T cells in the vicinity (<10 μm) of MHCII^{+}-expressing endothelial and epithelial cells in lungs. Data are collected from 10 different lung sections, zoomed in one area containing MHCII^{+} endothelial or epithelial structures. (**M**) Experimental layout for (N). i.v., intravenous. (**N**) Confocal microscopy images of lung sections from WT and CCR2$^{-/-}$ infected mice intravenously injected with TRITC-conjugated dextran ($n = 4$, two experiments). (**O**) Quantification of Evans blue concentration in BALF and lung to identify vascular leakage at day 8 after infection ($n = 2$ to 8, one experiment). For comparisons between two groups, Student's two-tailed *t* test was used. For comparisons between multiple groups, one-way or two-way ANOVA was used with multiple-comparison tests. *$P < 0.05$, **$P < 0.01$, ***$P < 0.001$, and ****$P < 0.0001$. Pictures are representative of more than six lungs analyzed. Error bars represent SEM. See also fig. S8.

Downloaded from https://www.science.org at Universit Catholique de Louvain on November 04, 2026

presence and absence of MOs (Fig. 1, K to M, and fig. S4), so we postulated that the PD-L1/PD-1 axis may inhibit hyperinflammation driven by cytotoxic CD4 T cells upon MuHV-4 infection. First, we confirmed that MuHV-4 infection triggers the recruitment of PD-L1/MHCII–coexpressing MOs and of PD-1–expressing CD4 T cells to the airways (Fig. 6, A to C). Second, we assessed the importance of the PD-L1/PD-1 pathway during MuHV-4 infection by comparing MuHV-4 infection in CCR2$^{-/-}$ mice and in WT mice, treated or not with anti–PD-L1/PD-1 neutralizing antibodies (Fig. 6D). Although this treatment did not affect the number of MOs in BALF or lung parenchyma (Fig. 6E), it induced severe disease associated with weight loss like that observed in CCR2$^{-/-}$ mice (Fig. 6F) and inflammatory cell infiltration in the lung upon MuHV-4 infection (Fig. 6G). Similar to what was observed in MuHV-4–infected CCR2$^{-/-}$ mice, we did not detect any difference in viral loads (Fig. 6H), suggesting that the PD-L1/PD-1 pathway protects from MuHV-4–induced immunopathology rather than limiting viral replication. To assess whether blocking the PD-L1/PD-1 axis recapitulates the cytotoxic features of CD4 T cells observed in CCR2$^{-/-}$ infected mice, we compared the phenotypic profiles of these cells between groups by flow cytometry and immunostaining. This analysis revealed a similar increase in GrzB, GrzA, perforin 1 (Prf1), and IFN-γ upon infection in CD4 T cells from MuHV-4 CCR2$^{-/-}$ and anti–PD-L1/PD-1–treated WT mice, in addition to a parallel release of GrzB and IFN-γ in BALF (Fig. 6, I to L). Last, in line with the exacerbated cytotoxic properties, we observed a loss of tissue integrity in CCR2$^{-/-}$ and in anti–PD-L1/PD-1–treated WT mice upon infection, as evidenced by a comparable increase in perivascular leakage of TRITC-dextran (Fig. 6, M and N). These data demonstrated a central role for MuHV-4–imprinted MOs in positioning CD4 T cells in close proximity and in providing them signals through the PD-L1/PD-1 axis that locally regulate their cytotoxicity.

Selective expression of PD-L1 by MOs is necessary to control virus-induced immunopathology

Our data support a key role of IL-10 and the PD-1/PD-L1 axis as regulators of MuHV-4–induced immunopathology, so we investigated possible connections in the regulation of these two pathways. We compared levels of expression of PD-L1 on MOs and of GrzB, GrzA, and IFN-γ on CD4 T cells in IL-10$^{-/-}$ mice (Fig. 7, A and B) and in CD4-cre IL-10$^{lox/lox}$ with respective littermates (Fig. 7, C and D). Both models showed that IL-10 deficiency increases IFN-γ production without affecting the cytotoxic properties of CD4 T cells, suggesting that IL-10 and PD-L1/PD-1 axes are two independent regulatory pathways that contribute to the protective phenotype in a complementary manner. We assessed the specific requirement of PD-L1–expressing MOs to prevent cytotoxic CD4 T cell–mediated damage. MOs and MO-derived AMs represent the main cell population in the airways expressing PD-L1 (Fig. 7, E and F). Because PD-1 can also be bound by PD-L2, and PD-1 blockade alone could induce inflammation independently of PD-L1–derived MOs, we compared the global inhibition of the PD-L1/PD-1 axis with individual PD-1 and PD-L1 blockades in MuHV-4–infected WT and CCR2$^{-/-}$ mice. We observed a similar weight loss between PD-L1–, PD-1–, or PD-L1/PD-1–treated WT mice (Fig. 7, G and H), in line with comparable production of GrzB, GrzA, and IL-10 by CD4 T cells (Fig. 7, I and J), supporting the statement that PD-L1 alone is sufficient to inhibit cytotoxic CD4 T cell–mediated immunopathology. We did not observe any notable differences in the weight loss or in the level of GrzB, GrzA, and IL-10 between untreated CCR2$^{-/-}$ and antibody-treated mice (Fig. 7, I and J), suggesting that MO-derived PD-L1 alone is sufficient to protect from cytotoxic CD4 T cell–mediated disease. To confirm this finding, we generated inducible conditional Ccr2-creER^{T2} PD-L1$^{lox/lox}$ mice (Fig. 7K). Ccr2-creER^{T2} PD-L1$^{lox/lox}$ mice treated with tamoxifen had great cell-specific excision of the PD-L1 gene, with >75% ablation on MO that was sufficient to trigger weight loss upon infection with MuHV-4 (Fig. 7L). In validation of weight loss curves, the specific lack of PD-L1 expression by MOs correlated with enhanced cytotoxic properties of CD4 T cells, as evidenced by the increased amounts of intracellular GrzA, Prf-1, and CD107a and by the increased release of GrzB in the airways (Fig. 7, M to P). Overall, these data confirm that MO-derived PD-L1 is specifically required to control the deleterious cytotoxic properties of CD4 T cells during MuHV-4 infection.

DISCUSSION

A large body of evidence has identified microorganisms, including resident viruses (*50*, *51*), as major drivers of immune imprinting. γHVs represent the archetype of persistent viruses that have coevolved as "old friends" with their host. Although the immune escape of γHVs from specific adaptive responses has been extensively studied (*52*, *53*), less is known about the subversion of innate immunity. We uncovered a critical role for γHV-imprinted MOs to recruit and establish regulatory cross-talk with CD4 T cells in the airways. By promoting the initial IL-10 release and inhibitory signals through checkpoint molecules, γHV-imprinted MOs prevent host damage by attracting CD4 T cells to their immediate vicinity and attenuating cytotoxic responses. γHVs have developed numerous strategies to produce asymptomatic infections in immunocompetent hosts, and this study demonstrates the essential role of MOs mobilized during the early stages of infection to regulate the balance between antiviral vigilance and immune tolerance.

MuHV-4 infection has been shown to train immunity against various heterologous infections (*54*, *55*). In addition to triggering regulatory pathways to dampen specific antiviral defenses, γHVs license CD8 (*56*), and potentially CD4, T cells to protect their own niche against heterologous pathogens. Here, we provide evidence supporting a role for γHV-imprinted MOs in the activation of CD4 T cells while finely regulating their cytotoxic and degranulation capacities. Because γHV-imprinted MOs persist for months with phenotypic changes (*10*), future studies are needed to examine whether equivalent regulation of cytotoxic CD4 T cells by these MO-derived AMs occurs in the context of long-term heterologous immunity. Interactome analysis revealed a dialogue between MuHV-4–imprinted MOs and CD4 T cells. A recent study also showed a requirement of CD8 T cells for the long-term training of MO-derived AMs in the context of adenovirus infection (*57*); thus, it would be interesting to assess whether MuHV-4–recruited CD4 T cells contribute similarly to imprint phenotypic alterations on MO-derived cells with lasting functional consequences.

CD4 T cells with cytotoxic functions are of increasing interest. Their presence in certain viral infections (*41*, *58*) including primary EBV infection (*59*), antitumor responses (*40*), or autoimmune disorders (*60*) has been associated either with disease aggravation (*61*) or with induction of protective immunity. Hence, supercentenarians exhibit a physiological accumulation of cytotoxic CD4 T cells, which may represent an essential adaptation to achieve exceptional longevity by sustaining efficient immune responses to infections (*62*). With

Downloaded from https://www.science.org at Universit Catholique de Louvain on November 04, 2026

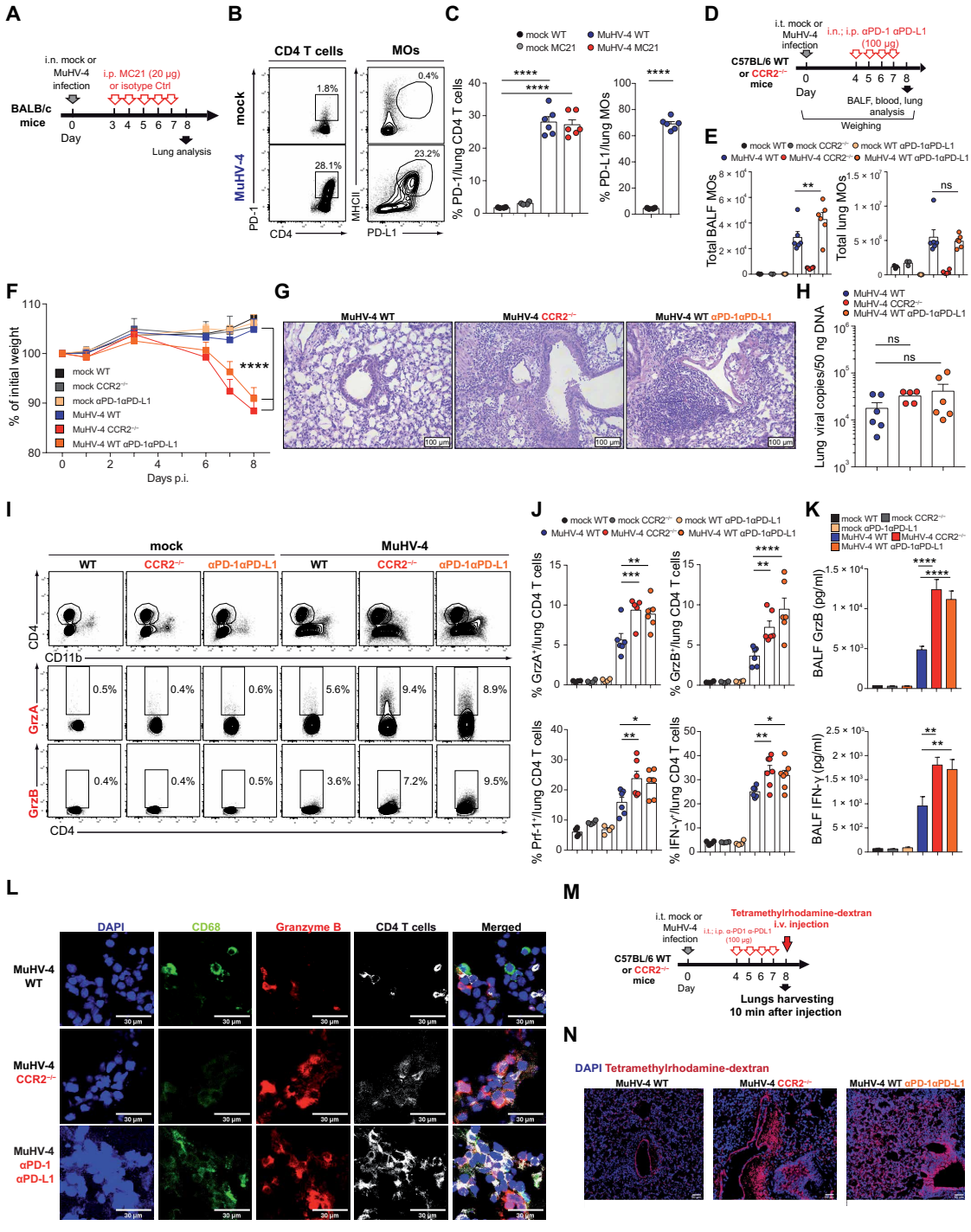


Fig. 6. The PD-L1/PD-1 axis is crucial for the control of the cytotoxic features of CD4 T cells and for the maintenance of peripheral immune homeostasis. (**A**) Experimental layout for (A) to (C). (**B** and **C**) FACS plots (B) and percentages (C) of PD-1–expressing CD4 T cells and PD-L1– and MHCII-coexpressing MOs at day 8 after infection ($n = 4$ to 6, three experiments). (**D**) Experimental layout for (E) to (L). (**E**) Numbers of MOs in BALF and lung ($n = 3$ to 6, three experiments). (**F**) Body weight as percentage of initial weight ($n = 4$ to 6, three experiments). (**G**) Histological analysis of lung sections at day 8 after infection stained with H&E ($n = 4$ to 6, one experiment). (**H**) MuHV-4 genome copies in lung at day 8 after infection ($n = 5$ to 6, one experiment). (**I**) FACS plots of lung CD4 T cells expressing GrzA and GrzB at day 8 after infection. Numbers in gates indicate means. (**J**) Percentages of GrzA-, GrzB-, Prf-, and IFN-γ–expressing lung CD4 T cells at day 8 after infection ($n = 4$ to 7, three experiments). (**K**) ELISA measurement of GrzB and IFN-γ in BALF at day 8 after infection ($n = 4$ to 19, three pooled experiments). (**L**) Confocal microscopy images of lung sections of mock- and MuHV-4–infected WT or CCR2$^{-/-}$ mice at day 8 after infection. (**M**) Experimental layout for (N). (**N**) Confocal microscopy images of lung sections from WT and CCR2$^{-/-}$ infected mice and intravenously injected with TRITC-dextran to identify vascular leakage at day 8 after infection ($n = 4$ to 6, one experiment). For comparisons between two groups, Student's two-tailed t test was used. For comparisons between multiple groups, one-way or two-way ANOVA was used with multiple-comparison tests. ns, not statistically different; *$P < 0.05$, **$P < 0.01$, ***$P < 0.001$, and ****$P < 0.0001$. Error bars represent SEM. Pictures are representative of more than six lungs analyzed.

Downloaded from https://www.science.org at Universit Catholique de Louvain on November 04, 2026

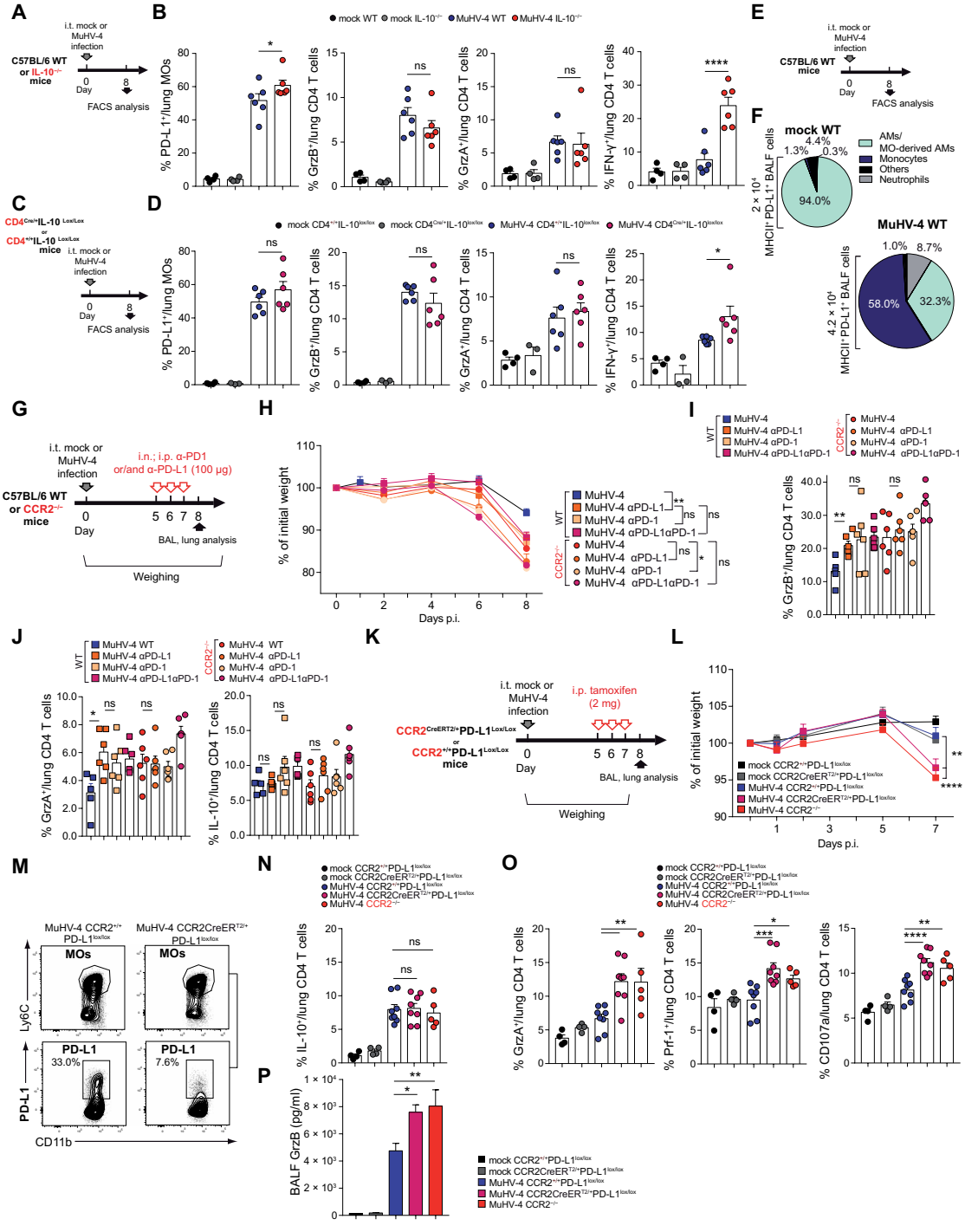


Fig. 7. Selective expression of PD-L1 by MOs is necessary to control virus-induced immunopathology. (**A**) Experimental layout for (B). (**B**) Percentages of PD-L1–expressing MOs and GrzB-, GrzA-, and IFN-γ–expressing lung CD4 T cells at day 8 after infection ($n = 4$ to 6, two experiments). (**C**) Experimental layout for (D). (**D**) Percentages of PD-L1–expressing MOs and GrzB-, GrzA-, and IFN-γ–expressing lung CD4 T cells at day 8 after infection ($n = 4$ to 6, one experiment). (**E**) Experimental layout for (F). (**F**) Pie charts depicting the average numbers and the proportions of the different PD-L1$^+$ cells in BALF at day 8 after infection. (**G**) Experimental layout for (H) to (J). (**H**) Body weight as percentage of initial weight ($n = 4$ to 6, one experiment). (**I**) Percentages of GrzB-expressing lung CD4 T cells at day 8 after infection ($n = 5$ to 6, one experiment). (**J**) Percentages of GrzA- and IL-10–expressing lung CD4 T cells at day 8 after infection ($n = 5$ to 6, one experiment). (**K**) Experimental layout for (L) to (P). (**L**) Body weight as percentage of initial weight ($n = 4$ to 14, one experiment). (**M**) FACS plots of lung MOs expressing PD-L1. Mean percentages are shown. (**N**) Percentages of IL-10–expressing lung CD4 T cells at day 8 after infection ($n = 4$ to 8, one experiment). (**O**) Percentages of GrzA-, Prf-1–, and CD107a-expressing lung CD4 T cells at day 8 after infection ($n = 4$ to 8, one experiment). (**P**) ELISA measurement of GrzB in BALF at day 8 after infection ($n = 4$ to 14, two pooled experiments). For comparisons between two groups, Student's two-tailed t test was used. For comparisons between multiple groups, one-way or two-way ANOVA was used with multiple-comparison tests. ns, not statistically different; $^*P < 0.05$, $^{**}P < 0.01$, $^{***}P < 0.001$, and $^{****}P < 0.0001$. Error bars represent SEM.

Downloaded from https://www.science.org at Universit Catholique de Louvain on November 04, 2026

regard to the ambivalent contribution of cytotoxic CD4 T cells to beneficial or pathogenic immune responses, deciphering the regulation of these super killer cells by MOs is of major importance.

IL-10 is a pleiotropic cytokine produced by multiple cell types that restrain immune activation in response to infection (*63*). Many herpesviruses manipulate the IL-10 pathway to facilitate host infection, latency establishment, and viral dissemination (*64*, *65*). Consistent with previous findings (*66*), we identified the CD4 T cell population as the major source of IL-10 in the airways during the early stages of MuHV-4 infection. In addition to classical Foxp3$^+$ T_{reg} CD4 T cells, we noticed a marked enrichment of Foxp3$^-$ IL-10$^+$ effector CD4 T cells. Furthermore, by infecting IL-10$^{-/-}$ mice or CD4-cre IL-10$^{lox/lox}$ with MuHV-4, we observed that an absence of T cell–derived IL-10 during acute infection disrupts the host-virus interaction and triggers a massive neutrophil infiltration and an uncontrolled release of proinflammatory cytokines including IFN-γ. In addition to dampening the overall inflammation, IL-10 produced by CD4 T cells may be part of an autocrine feedback loop, regulating directly their effector properties, and especially their production of IFN-γ, as described for other infections (*67*).

In parallel to the IL-10–dependent regulatory pathway, we found the specific expression of PD-L1 by MOs recruited in response to γHV infection as an important adaptive mechanism that minimizes immunopathology. Overexpression of immune checkpoint proteins leading to T cell exhaustion is a key immune evasion strategy exploited by many tumor cells. Because "old friend viruses" have converged to exploit a similar immune evasion strategy, a thorough understanding of the mechanisms regulating PD-L1/PD-1 signaling could provide important insights for both antitumor and antiviral therapies. The impact of PD-L1/PD-1 axis in chronic infection is well described, whereas its role during the acute phase of viral infection is less clear (*68*). Given the diversity of biological functions of the PD-L1/PD-1 pathway, including suppression of T cell receptor or costimulatory signaling (*69*) and the regulation of development, maintenance, and function of IL-10–producing T cells (*70*), further studies are needed to reveal the precise molecular cascades mediated by PD-L1–expressing MOs during MuHV-4 infection. Our results highlight the importance of PD-L1 expression by MOs in controlling the cytotoxic profile of CD4 T cells and in modulating their degranulation. Because cytotoxic CD8 T cells can also express PD-1, it would be of great interest to study whether a similar regulation of PD-1$^+$ CD8 T cells by PD-L1$^+$ MOs takes place and limits tissue damage after MuHV-4 infection.

This research also provides substantial insights for clinical findings in human. Notable observations are the severe immune-related adverse events (irAEs) that occur in some patients treated with checkpoint inhibitors and that exhibit uncontrolled T cell activation (*71*). Although the molecular basis of irAEs is poorly defined, EBV-induced cytotoxic CD4 T cells have been pointed out as the main culprit in anti–PD-L1/PD-1–associated encephalitis, supporting a link between γHV infections and irAEs. In other contexts, EBV infection has been identified as a major risk factor to develop severe immunopathologies such as multiple sclerosis or hemophagocytic lymphohistiocytosis (*72*). Therefore, it would be interesting to determine whether a possible failure in the MO-CD4 T cell synergy is involved in the development of such immunopathological manifestations in humans.

The early age of γHV infection and the multiple confounding factors encountered during life make it very complicated to study γHV immune imprinting in humans. In contrast, mice serve as valuable animal models of γHV infection for which genetic and microbiological variables can be tested. Although one of the limitations of the study is that it is confined on the mouse model, it will be interesting in the future to investigate similar immune signatures and regulatory pathways in human samples. Furthermore, because this work has only focused on the importance of the MO-CD4 regulatory axis, further studies are needed to determine the importance of a similar regulatory interplay between MOs and cytotoxic CD8 T cells.

Overall, this work has dissected the complex interplay between MuHV-4–imprinted MOs and CD4 T cells recruited in the airways during γHV infection. This study has revealed the importance of the IL-10 and PD-L1/PD-1 signaling pathways in curbling pathological inflammation before the development of severe respiratory injury and systemic disease. Although PD-1 agonism deserves increased attention in the control of autoimmunity (*73*), this study may open new perspectives, beyond the context of γHV infection, in the therapeutic management of various viral immunopathologies.

MATERIALS AND METHODS

Study design

This study was designed to understand the function of Ly6C^{hi} MOs in modulating inflammation induced by respiratory γHV infection. To this end, we compared the development of the acute post-infection immune response between WT, MC21-depleted, and MO-deficient (CCR2$^{-/-}$) mice. To clarify the cellular and molecular mechanisms, we generated genetically modified mice. Mechanisms of immunopathology were investigated during peak disease symptoms in mice at day 8 after infection. Endpoint analyses included flow cytometry, ELISA, quantitative polymerase chain reaction (qPCR), scRNA-seq, and histology. All experiments used randomly assigned mice without investigator blinding. All data points and *n* values reflect biological replicates. The specific numbers and genotypes of the mice and the statistics performed are included in the legend of each figure.

Mice

This study was conducted in strict accordance with guidelines of the European Convention for the Protection of Vertebrate Animals used for Experimental and other Scientific Purposes (CETS 123). The protocol was approved by the Committee on the Ethics of Animal Experiments of ULiège (permit numbers 2015 and 2215). All efforts were made to minimize suffering, and all inoculations were performed under isoflurane anesthesia. Dissections were performed after euthanasia of the animals.

Female BALB/c, C57BL/6 WT, C57BL/6 CD45.1, and C57BL/6 albino mice were purchased from Charles River (L'Arbresle, France). CCR2$^{-/-}$, IL-10$^{-/-}$, IL-10$^{lox/lox}$, IL-10-β-lactamase reporter (ITIB), and CD4-Cre mice were provided by F. Bureau, T. Marichal, and C. Desmet (ULiège). These mice are available at the Jackson Laboratory or were described elsewhere (*38*). PD-L1$^{fl/fl}$ mice (CD274^{tm1Pfal}) were originally obtained from P.G.F. (Trinity Biomedical Sciences Institute, Dublin). Ccr2-creER^{T2} mKate2 mice (*37*) were originally obtained from B. Becher (Institute of Experimental Immunology, Zurich University). All cre strains were heterozygous. Six- to 8-week-old female littermates were randomly assigned to experimental groups. During experiments, four to five female mice were cohoused per cage, and food and water were provided ad libitum. All the animals were

Downloaded from https://www.science.org at Universit Catholique de Louvain on November 04, 2026

bred and/or housed in the ULiège Department of Infectious Diseases or at GIGA animal facility.

Cell lines and cell culture

BHK-21 (baby hamster kidney) fibroblasts (American Type Culture Collection, CCL-10, RRID:CVCL_1915) were cultured in Dulbecco's modified Eagle's medium, supplemented with 2 mM glutamine, penicillin (100 U/ml), streptomycin (100 mg/ml), and 10% fetal calf serum (FCS) in 5% CO_2 at a 37°C incubator. Cells were free of mycoplasma contamination.

Viruses

The WT MHV-68 strain of MuHV-4 (*74*) and a luciferase-expressing MuHV-4 strain (*75*) (MuHV-4-Luc) were used and propagated on BHK-21 cells. Cells and supernatant were harvested at about 4 days after infection (~85% of lysis), and debris were removed by low-speed centrifugation (1000*g*, 10 min, 4°C). Virions present in the supernatant were harvested by ultracentrifugation (100,000*g* for 2 hours at 4°C) and purified through a 30% (w/v) sucrose cushion (100,000*g* for 2 hours at 4°C), washed in phosphate-buffered saline (PBS) before being stored in PBS at −80°C. Viral titers were determined by plaque assay on BHK-21 cells. Briefly, BHK-21 cell monolayers were incubated with 10-fold dilution of viral stock at 37°C and 5% CO_2 for 3 hours. Inoculum was then replaced by semisolid medium containing 0.6% carboxymethylcellulose. Cells were further incubated for 4 days and then fixed in 4% paraformaldehyde (PFA) and stained for plaque counting.

Infection model

Intranasal or intratracheal administration of virions was performed under isoflurane anesthesia, with 1×10^4 plaque-forming units (PFU) of MuHV-4 WT or MuHV-4-Luc in 50 μl of PBS. As control, mock-infected mice received 50 μl of PBS. Clinical scoring was performed after infection, based on a customized clinical evaluation grid.

For MuHV-4-Luc infection, light emission was monitored by in vivo bioluminescence imaging using the IVIS Spectrum In Vivo Imaging System (PerkinElmer) after D-luciferin (150 mg/kg of body weight; PerkinElmer) intraperitoneal injection. Living Image v4.1 software (PerkinElmer) was used to obtain the total flux (photons per second) using a fixed-sized region of interest or average radiance (photons per second per square centimeter per steradian).

Viral quantification

Viral genome loads were measured using a TaqMan-based real-time PCR (CFX). DNA was extracted from lungs using a QIAamp DNA Mini kit (Qiagen), and 50 ng per sample was used in iQ Supermix (Bio-Rad) to amplify a MuHV-4–specific sequence (genomic coordinates 43,015 to 43,138, NC_001826.2): gene ORF25 with primers 5′-atggtatagccgcctttgtg-3′ (ORF25fwd) and 5′-acaagtggatgaagggttgc-3′ (ORF25rev) and probe 5′-6-carboxyfluorescein [FAM]-caaccactg-gatcagcataaaacttatgaa-black hole quencher [BHQ1]-3′. Standard curves were obtained using pGEMT-easy (Promega) plasmid templates in which MuHV-4 ORF25 was cloned.

Respiratory mechanics

Mice were anesthetized with sodium pentobarbital (Nembutal) intraperitoneally at a dose of 50 mg/kg. The trachea was isolated via dissection of the neck area and cannulated using an 18-gauge blunt metal cannula (typical resistance of 0.18 cmH_2Os/ml), which was secured in place with a nylon suture. The mouse was then connected to the flexiVent computer-controlled piston ventilator (SCIREQ) via the cannula, which was attached to the FX adaptor Y-tubing. Mice were ventilated using default settings for mice, which consisted of a positive end expiratory pressure at 3 cmH_2O, a tidal volume of 10 ml/kg, a respiratory rate of 150 breaths per minute, and a fraction of inspired oxygen of 0.21 (that is, room air). Respiratory mechanics were assessed using the forced oscillation technique, using the latest version of the flexiVent operating software (flexiWare version 8.1.3).

Antigen-specific antibody titers

Nunc Maxisorp ELISA plates (Nalgene Nunc) were coated overnight at 4°C with MuHV-4 virions [10^6 PFU/ml of carbonate buffer (pH 9.5) containing 0.1% Triton X-100] before being incubated for 1 hour in wash/blocking buffer [0.1% Tween 20 and 3% bovine serum albumin (BSA) in PBS] at room temperature (RT). Plates were then incubated with mouse sera (serial dilutions) in wash/blocking buffer for 2 hours at RT. After incubation for 1 hour at RT with biotinylated goat anti-mouse IgG or IgG2A, detection was performed using streptavidin–alkaline phosphatase in wash/blocking buffer for 1 hour at RT. Chromogenic reaction was performed using *p*-nitrophenylphosphate (Sigma-Aldrich) and stopped in 1 M NaOH before absorbance was read at 405 nm using an iMark ELISA plate reader (Bio-Rad).

Antibody-mediated in vivo depletion

$CCR2^+$ MOs were systemically depleted using the rat anti-mouse CCR2 antibody, MC21 (*23*). Mice were injected intraperitoneally with 20 or 100 μg of MC21 or isotype control (dissolved in 200 μl of PBS) at the indicated times after infection and were weighed until euthanasia.

Neutrophils were depleted by intraperitoneal injection of 100 μg of anti-Ly6G antibody (InVivoMab, anti-mouse Ly6G, clone 1A8, BioXCell) at the indicated times after infection. PD-1/PD-L1 axis was blocked by intranasal and intraperitoneal injection of 100 μg of anti–PD-1 neutralizing antibody (InVivoMab, anti-mouse PD-1, clone RMP1-14, BioXCell) and/or anti–PD-L1 neutralizing antibody (InVivoMab, anti-mouse PD-L1, clone 10F.9G2, BioXCell).

Tamoxifen treatment

Tamoxifen (Sigma-Aldrich, T5648) was dissolved in corn oil to 10 mg/ml and administered in 200-μl doses via intraperitoneal injection (2 mg per dose) at the indicated times after infection.

BAL, cytology, and cytokine measurement

After euthanasia, the trachea was catheterized and bronchoalveolar lavage was performed by two consecutive flushes of the lungs with 1 ml of ice-cold PBS containing cOmplete Protease Inhibitor Cocktail (Roche). One tablet of inhibitor cocktail was dissolved in 50 ml of ice-cold PBS. Cell density in BALF was evaluated using a hemocytometer after Tuerk solution staining (Sigma-Aldrich). Cytokine production (IFN-γ and GrzB) was measured by specific ELISA (Ready-SET-Go, eBioscience) according to the manufacturer's instructions.

In vivo lung vascular permeability assay

TRITC assay

Mice were intravenously injected with TRITC-dextran 10 min before euthanasia (50 mg/kg; Thermo Fisher Scientific, D3307). After

Downloaded from https://www.science.org at Universit Catholique de Louvain on November 04, 2026

euthanasia, lungs were perfused, collected, fixed in 4% PFA-PBS overnight, and embedded in paraffin. Five-micrometer-thick sections were deparaffinized, rehydrated, and mounted with 4′,6-diamidino-2-phenylindole (DAPI) Fluoromount-G. Sections were imaged using an OLYMPUS VS200 ASW 3.2 scanner and analyzed using the OLYMPUS OlyVIA software.

Miles assay

Mice were intravenously injected with Evans blue (50 mg/kg; Sigma-Aldrich, E2129) 30 min before euthanasia. After euthanasia, BALF was collected as described. Lungs were perfused before harvesting. Evans blue concentrations from lungs and BALF were measured with a spectrophotometer (620 nm) after 24 hours of formamide extraction.

Lung histology

Lungs were fixed in 5% formalin, paraffin-embedded, and cut into 5-μm sections that were then stained with hematoxylin and eosin (H&E) before analysis.

Cell suspension preparations from organs

To harvest lung cells, mice were perfused with ice-cold PBS through the right ventricle. Then, lung lobes were collected into a C-tube (Miltenyi) containing complete Hanks' balanced salt solution medium, collagenase D (1 mg/ml; Roche), and deoxyribonuclease I (50 μg/ml; Roche). These lung lobes were processed with a gentleMACS dissociator (Miltenyi) and, finally, were incubated for 30 min at 37°C. BM cells were obtained from adult mice by crushing the femurs and tibiae. Blood was collected by cardiac puncture and was immediately suspended in ice-cold PBS complemented with 5 mM EDTA. Suspensions of cells were finally washed and treated for erythrocyte lysis (1× RBC Lysis Buffer, eBioscience). To obtain MLN cells, MLNs were harvested after euthanasia, and single-cell suspensions were prepared by crushing them using a sterile syringe plunger. For all preparations, cells were finally strained through a 70-μm filter. Cell density was evaluated using a hemocytometer after trypan solution staining (Sigma-Aldrich).

MHC-tetramer stainings

Lung cells were processed as described above from C57BL/6 WT and $CCR2^{-/-}$ mice. Cells were incubated with BV421-conjugated tetramers H-$2D^b$-$ORF6^{487–495}$ (AGPHNDMEI, 90 nM) and H-$2K^b$-$ORF61^{521–531}$ (TSINFVKI, 45 nM) (National Institutes of Health Tetramer Core Facility) for 30 min at RT before further staining. Samples were analyzed on a BD LSRFortessa X-20 flow cytometer (BD Biosciences).

Assessment of IL-10 expression in ITIB mice

To assess IL-10 expression using IL-10-β-lactamase reporter ITIB mice, BALF and lung cells isolated from IL-10-β-lactamase reporter ITIB and control WT mice were resuspended in a CCF4-AM (Thermo Fisher Scientific, catalog no. K1028)–containing solution supplemented with probenecid (Thermo Fisher Scientific, catalog no. P36400) prepared according to the manufacturer's instructions and incubated for 90 min at 29°C. CCF4-AM is a lipophilic ester derivative that consists of a cephalosporin core bridging a 7-hydroxycoumarin to a fluorescein. Exciting intact CCF4 at 405 nm induces fluorescence resonance energy transfer (FRET) from the coumarin to the fluorescein that subsequently emits green light. IL-10 expression is evaluated by detection of a 450-nm fluorescence (blue fluorescent product of the cleaved CCF4 substrate by β-lactamase, under the control of the IL-10 gene promoter) in CCF4-loaded cells. Protocol for flow cytometry surface staining was classically used before analysis. CCF4-loaded WT cells were used as negative controls.

Analysis of cytokine concentrations

Two different panels were used: 13-plex antivirus mouse panel of cytokines/chemokines and 13-plex customized mouse panel from LEGENDplex bead array (BioLegend) according to the manufacturer's protocol on BALF samples. All samples were run on a BD LSRFortessa X-20 flow cytometer, and analysis was performed using LEGENDplex analysis software (BioLegend).

Flow cytometry

Labeling of single-cell suspension was performed on ice in PBS containing 2% FCS and 2 mM EDTA. Cells were first incubated for 20 min with a purified rat IgG2a anti-mouse CD16/CD32 antibody (BioLegend) to block Fc binding. Flow cytometry staining was performed for 30 min at 4°C in PBS containing 0.5% BSA with various panels of fluorochrome-conjugated antibodies. The gating strategy to identify the different cell populations included successive forward- and side-scatter gating, exclusion of multiplets, and selection of living cells with the viability markers Zombie Aqua or Violet (BioLegend). The Foxp3 Transcription Factor Staining kit was purchased from eBioscience and used for intranuclear staining. Samples were processed on a BD LSRFortessa X-20 equipped with 50-mW violet 405-nm, 50-mW blue 488-nm, 50-mW yellow-green 561-nm, and 40-mW red 633-nm lasers and an ND1.0 filter in front of the FSC (forward scatter) photodiode. Gating strategy used to identify MO and CD4 T cell populations is described in the Supplementary Materials (fig. S9).

Ex vivo restimulation and cytokine production

For IL-10 intracellular staining, single-cell suspensions were stimulated in complete RPMI medium containing 2 μM monensin and 2 μM brefeldin (BD Biosciences) and 50 μM β-mercaptoethanol (Life Technologies) for 4 hours at 37°C. Depending on conditions, we added LPS (10 ng/ml; Sigma-Aldrich) for MO intracellular staining or purified CD28 antibody (1 μg/ml; BioLegend) and purified CD3ε antibody (2 μg/ml; BioLegend) for CD4 T cell intracellular staining. For IFN-γ intracellular staining, single-cell suspensions were stimulated in complete RPMI medium containing 2 μM monensin and 2 μM brefeldin (BD Biosciences) and 50 μM β-mercaptoethanol (Life Technologies) for 4 hours at 37°C with purified CD28 antibody (1 μg/ml; BioLegend) and purified CD3ε antibody (2 μg/ml; BioLegend). For GrzA and GrzB intracellular stainings, single-cell suspensions were accumulated in complete RPMI medium containing 2 μM monensin and 2 μM brefeldin (BD Biosciences) and 50 μM β-mercaptoethanol (Life Technologies) for 4 hours at 37°C. For Prf-1 intracellular staining, single-cell suspensions were stimulated in complete RPMI medium containing 2 μM monensin and 2 μM brefeldin (BD Biosciences) and 50 μM β-mercaptoethanol (Life Technologies) for 4 hours at 37°C with purified CD28 antibody (1 μg/ml; BioLegend), purified CD3ε antibody (2 μg/ml; BioLegend), purified CD49d antibody (1 μg/ml; BioLegend), and allophycocyanin anti-mouse CD107a (0.5 μg/ml; LAMP-1) antibody (BioLegend).

Immunostainings and confocal microscopy analyses

Lungs were collected from C57BL/6 WT and $CCR2^{-/-}$ mice. After euthanasia, 1 ml of OCT (optimal cutting temperature) compound (Scigen) was injected intratracheally and lungs were embedded in

Downloaded from https://www.science.org at Universit Catholique de Louvain on November 04, 2026

OCT compound before freezing in blocks. Sections were processed on a Leica CM3050S cryomicrotome (7 to 10 μm), dried on slides for 30 min, and kept at −80°C until staining. Tissue sections were then fixed in 4% PFA for 10 min at RT, permeabilized or not in a solution composed of 0.4% (v/v) Triton X-100 (Sigma-Aldrich) and 125 mM glycine (Sigma-Aldrich) for 10 min at RT, and blocked in PBS containing 5% (v/v) BSA (Sigma-Aldrich) for 1 hour at RT. Sections were first stained with the following primary antibodies depending on the panels: rat IgG2a anti-mouse CD68 (1:50; Thermo Fisher Scientific; 14-0681-82) or polyclonal rabbit IgG anti-mouse MHCII (1:500; Invitrogen, PA5-116876), rat IgG2b anti-mouse CD4 (1:50; Thermo Fisher Scientific, 14-0041-82), and polyclonal goat IgG anti-mouse GrzB (1:100; R&D Systems, AF1865) for 2 hours at RT. Sections were then stained with the following secondary antibodies: anti-rat IgG2a AF488 (1:500; Abcam; ab172332) or anti-rabbit IgG AF555 (1:1000; Thermo Fisher Scientific; A-21428), anti-rat IgG2b AF647 (1:500; BioLegend; 408208), and NL557-conjugated anti-goat antibody (1:1000; R&D Systems; NL001) for 1 hour at RT. Cell nuclei were counterstained with DAPI (BioLegend) for 10 min at RT. Sections were mounted with Prolong Diamond Antifade Mountant (Thermo Fisher Scientific) and stored for at least 5 hours at RT. Samples were rinsed three times in PBS between each of the above-mentioned steps. Regarding GrzB staining, two distinct immunofluorescence staining protocols were used: the classical protocol, as described above including the permeabilization and staining steps with Triton X-100, and an alternative protocol excluding permeabilization steps and the use of Triton X-100. The alternative surface labeling process allows the distinction of proteins expressed only at the level of the cell surface and released in the extracellular medium separately from the proteins expressed within the cell. Images were acquired on a Leica TCS SP5 Confocal Laser Scanning Microscope and analyzed using the Fiji software. For the quantification of lung GrzB$^+$ CD4 T cells in the vicinity of MHCII$^+$ endothelial and epithelial cells, GrzB$^+$ CD4 T cells were quantified and categorized as "being in close contact with MHCII$^+$ endothelial and epithelial cells," when the distance between the two was <10 μm. Quantification was performed on 10 different areas on lung sections for each condition.

Generation of BM chimeras

BM chimeras were constructed by exposure of C57BL/6 CD45.1.2$^+$ mice to a whole-body lethal irradiation protocol (Gammacell 40 Exactor, 6 Gy). The next day, recipient mice were reconstituted by intravenous injection of 5×10^6 BM cells isolated from femurs and tibias of donor CD45.1$^+$ WT and CD45.2$^+$ IL-10$^{-/-}$ or CCR2$^{-/-}$ mice and mixed at a 1:1 ratio. From 1 week before to 3 weeks after irradiation, mice were given broad-spectrum antibiotherapy (Emdotrim 10% SOL, Emdoka). Mice were left untreated for 8 weeks to allow complete reconstitution, and chimerism of the different blood leukocyte populations was then confirmed by flow cytometry.

Single-cell RNA sequencing

Library preparations for single-cell immune profiling, sequencing, and postprocessing of the raw data were performed at the GIGA-Genomics Core Facility (Belgium). Sorted cells were washed with 1× PBS (calcium and magnesium free) containing 0.04% (w/v) BSA (400 μg/ml). BALF and lung cells were pooled together within each condition after cell hashing with barcoded antibodies (BioLegend). We equalized numbers of cells between conditions for scRNA-seq profiling, cell concentration was adjusted to 1000 total cells/μl, and 16,000 cells were loaded on Chromium Controller (10x Genomics). Samples were further processed for droplet-based RNA-seq, and libraries were prepared using Chromium Single Cell 3′ Reagent Kits v3 according to the manufacturer's protocol (10x Genomics). Amplified complementary DNA (cDNA) quality controls were performed with an Agilent bioanalyzer (Agilent), and final library profile was checked on Qiaxcel (Qiagen). Sequencing libraries were loaded an Illumina NovaSeq sequencer with a NovaSeq SP 100 v1 kit (Illumina, CA, USA) using the following read lengths: 28 base pairs (bp) for Read1 (18-bp barcode + 10-bp randomer), 8 bp for sample index, and 88 bp for Read2. Library quantification was processed with a KAPA Library quantification kit (KAPA Biosystems). Gene counts were obtained by aligning reads to the mm10 genome using CellRanger software (10x Genomics).

Analysis of scRNA-seq samples

CellRanger software (v.3.0.2) (10x Genomics) was used to demultiplex Illumina BCL files to FASTQ files (cellranger mkfastq); to perform alignment to mouse GRCm38/mm10 genome, filtering, and unique molecular identifier (UMI) counting; and to produce gene-barcode matrices (cellranger count). Subsequent analysis used R (v.4.1.0) and the R package Seurat (v.4.0.3). First, individual datasets were read into R as count matrices and converted into Seurat objects (min.cells = 3, min.features = 200 genes), and cells with ≤200 distinct genes and ≥10% mitochondrial reads were filtered out. Each matrix was integrated using FindIntegrationAnchors with anchor.features = 2000 and dims = 1:30 options. On the basis of an elbow plot, principal components (PCs) 1:20 were used in the subsequent analyses.

Cell type identification

Cells were grouped in 82 metacells using the FindCluster function of Seurat with a resolution of 10. Identification was made using the SingleR package.

UMAP representation

Nonlinear dimensional reduction with UMAP was used to visualize the datasets, using the top 20 PCs. The integrated object of the data of all conditions was scaled on the top 2000 variables used for the integration. The clusters were calculated using the FindClusters function with a resolution of 0.10.

BubbleGUM analysis

BubbleGUM (*47*) analysis was used as described previously with default settings, and the gene sets (containing between 20 and 500 genes) from Gene Ontology and gene set were arbitrarily determined on the basis of the literature (*10*). The results with a false discovery rate (FDR) of ≤0.25 were considered as significant.

NicheNet

To study intercellular communication, the NicheNet package for R was used (*36*). The top 20 ligands were kept, and "mouse" was selected for option organism in the function nichenet_seuratobj_aggregate.

Potential interaction scores

To link NicheNet analysis with our data, we created the potential interaction score based on the average expression of ligand × average expression of receptor/target gene × weight of the interaction provided by the NicheNet package. The average expression of a gene is based on the Seurat package default calculation: $\log_1 P$ (RNA count for this gene/total RNA count × 10,000). The weight of an interaction is retrieved from the corresponding databases of the NicheNet package.

Downloaded from https://www.science.org at Universit Catholique de Louvain on November 04, 2026

Circlize

The circular visualization was made with the R package circlize (*76*). The intensity of the color of the link between ligands and receptors is proportional to the score of the ligand-receptor link for each sender cell type (alpha from 0.25 to 1). The genes were chosen on the basis of the literature.

Statistical analysis

All statistical analyses were performed using GraphPad Prism software. Results were expressed as means ± SEM. Student's two-tailed *t* test was done to compare two groups. For comparisons of means between more than two experimental groups, two-way analysis of variance (ANOVA) or one-way ANOVA was used as appropriate. $P > 0.05$ was considered not significant (ns); $P < 0.05$ was considered significant; $^{*}P < 0.05$; $^{**}P < 0.01$; $^{***}P < 0.001$; $^{****}P < 0.0001$. Each dot represents one mouse. For scRNA-seq data, all statistical analyses were performed in R (v.4.1.0) and with various Bioconductor packages.

SUPPLEMENTARY MATERIALS

www.science.org/doi/10.1126/sciimmunol.abn3240
Figs. S1 to S9
Tables S1 and S2
Data file S1
MDAR Reproducibility Checklist

View/request a protocol for this paper from *Bio-protocol*.

REFERENCES AND NOTES

1. Y. Belkaid, T. W. Hand, Role of the microbiota in immunity and inflammation. *Cell* **157**, 121–141 (2014).
2. C. M. Lloyd, B. J. Marsland, Lung homeostasis: Influence of age, microbes, and the immune system. *Immunity* **46**, 549–561 (2017).
3. J. L. Schultze, A. C. Aschenbrenner, COVID-19 and the human innate immune system. *Cell* **184**, 1671–1692 (2021).
4. C. Shi, E. G. Pamer, Monocyte recruitment during infection and inflammation. *Nat. Rev. Immunol.* **11**, 762–774 (2011).
5. M. Merad, J. C. Martin, Pathological inflammation in patients with COVID-19: A key role for monocytes and macrophages. *Nat. Rev. Immunol.* **20**, 355–362 (2020).
6. E. Cesarman, Gammaherpesviruses and lymphoproliferative disorders. *Annu. Rev. Pathol. Mech. Dis.* **9**, 349–372 (2014).
7. E. S. Barton, D. W. White, J. S. Cathelyn, K. A. Brett-McClellan, M. Engle, M. S. Diamond, V. L. Miller, H. W. Virgin IV, Herpesvirus latency confers symbiotic protection from bacterial infection. *Nature* **447**, 326–329 (2007).
8. D. W. White, R. Suzanne Beard, E. S. Barton, Immune modulation during latent herpesvirus infection. *Immunol. Rev.* **245**, 189–208 (2012).
9. E. Barton, P. Mandal, S. H. Speck, Pathogenesis and host control of gammaherpesviruses: Lessons from the mouse. *Annu. Rev. Immunol.* **29**, 351–397 (2011).
10. B. Machiels, M. Dourcy, X. Xiao, J. Javaux, C. Mesnil, C. Sabatel, D. Desmecht, F. Lallemand, P. Martinive, H. Hammad, M. Guilliams, B. Dewals, A. Vanderplasschen, B. N. Lambrecht, F. Bureau, L. Gillet, A gammaherpesvirus provides protection against allergic asthma by inducing the replacement of resident alveolar macrophages with regulatory monocytes. *Nat. Immunol.* **18**, 1310–1320 (2017).
11. M. H. Askenase, S.-J. Han, A. L. Byrd, D. MoraisdaFonseca, N. Bouladoux, C. Wilhelm, J. E. Konkel, T. W. Hand, N. Lacerda-Queiroz, X.-z. Su, G. Trinchieri, J. R. Grainger, Y. Belkaid, Bone-marrow-resident NK cells prime monocytes for regulatory function during infection. *Immunity* **42**, 1130–1142 (2015).
12. N. V. Serbina, E. G. Pamer, Monocyte emigration from bone marrow during bacterial infection requires signals mediated by chemokine receptor CCR2. *Nat. Immunol.* **7**, 311–318 (2006).
13. M. Mack, J. Cihak, C. Simonis, B. Luckow, A. E. I. Proudfoot, J. Plachý, H. Brühl, M. Frink, H.-J. Anders, V. Vielhauer, J. Pfirstinger, M. Stangassinger, D. Schlöndorff, Expression and characterization of the chemokine receptors CCR2 and CCR5 in mice. *J. Immunol.* **166**, 4697–4704 (2001).
14. T. Lenac Rovis, P. Kucan Brlic, N. Kaynan, V. Juranic Lisnic, I. Brizic, S. Jordan, A. Tomic, D. Kvestak, M. Babic, P. Tsukerman, M. Colonna, U. Koszinowski, M. Messerle, O. Mandelboim, A. Krmpotic, S. Jonjic, Inflammatory monocytes and NK cells play a crucial role in DNAM-1–dependent control of cytomegalovirus infection. *J. Exp. Med.* **213**, 1835–1850 (2016).
15. C. D. Conrady, M. Zheng, N. A. Mandal, N. van Rooijen, D. J. J. Carr, IFN-α-driven CCL2 production recruits inflammatory monocytes to infection site in mice. *Mucosal Immunol.* **6**, 45–55 (2012).
16. M. Rolot, A. M. Dougall, A. Chetty, J. Javaux, T. Chen, X. Xiao, B. Machiels, M. E. Selkirk, R. M. Maizels, C. Hokke, O. Denis, F. Brombacher, A. Vanderplasschen, L. Gillet, W. G. C. Horsnell, B. G. Dewals, Helminth-induced IL-4 expands bystander memory CD8+ T cells for early control of viral infection. *Nat. Commun.* **9**, 4516 (2018).
17. H. Xiong, E. G. Pamer, Monocytes and infection: Modulator, messenger and effector. *Immunobiology* **220**, 210–214 (2015).
18. J. V. Camp, C. B. Jonsson, A role for neutrophils in viral respiratory disease. *Front. Immunol.* **8**, 550 (2017).
19. Q. Liu, Y. H. Zhou, Z. Q. Yang, The cytokine storm of severe influenza and development of immunomodulatory therapy. *Cell. Mol. Immunol.* **13**, 3–10 (2016).
20. Y. Tang, J. Liu, D. Zhang, Z. Xu, J. Ji, C. Wen, Cytokine storm in COVID-19: The current evidence and treatment strategies. *Front. Immunol.* **11**, 1708 (2020).
21. A. L. Croxford, M. Lanzinger, F. J. Hartmann, B. Schreiner, F. Mair, P. Pelczar, B. E. Clausen, S. Jung, M. Greter, B. Becher, The cytokine GM-CSF drives the inflammatory signature of CCR2+ monocytes and licenses autoimmunity. *Immunity* **43**, 502–514 (2015).
22. H. Bouabe, Y. Liu, M. Moser, M. R. Bosl, J. Heesemann, Novel highly sensitive IL-10–β-lactamase reporter mouse reveals cells of the innate immune system as a substantial source of IL-10 in vivo. *J. Immunol.* **187**, 3165–3176 (2011).
23. C. Bosteels, K. Neyt, M. Vanheerswynghels, M. J. van Helden, D. Sichien, N. Debeuf, S. De Prijck, V. Bosteels, N. Vandamme, L. Martens, Y. Saeys, E. Louagie, M. Lesage, D. L. Williams, S. C. Tang, J. U. Mayer, F. Ronchese, C. L. Scott, H. Hammad, M. Guilliams, B. N. Lambrecht, Inflammatory type 2 cDCs acquire features of cDC1s and macrophages to orchestrate immunity to respiratory virus infection. *Immunity* **52**, 1039–1056.e9 (2020).
24. C. Mesnil, C. M. Sabatel, T. Marichal, M. Toussaint, D. Cataldo, P.-V. Drion, P. Lekeux, F. Bureau, C. J. Desmet, Resident CD11b+Ly6C– lung dendritic cells are responsible for allergic airway sensitization to house dust mite in mice. *PLOS ONE* **7**, e53242 (2012).
25. Y. Ohmori, T. A. Hamilton, IL-4-induced STAT6 suppresses IFN-gamma-stimulated STAT1-dependent transcription in mouse macrophages. *J. Immunol.* **159**, 5474–5482 (1997).
26. R. A. Rahimi, A. D. Luster, Chemokines: Critical regulators of memory T cell development, maintenance, and function. *Adv. Immunol.* **138**, 71–98 (2018).
27. R. Tokunaga, W. Zhang, M. Naseem, A. Puccini, M. D. Berger, S. Soni, M. McSkane, H. Baba, H.-J. Lenz, CXCL9, CXCL10, CXCL11/CXCR3 axis for immune activation—A target for novel cancer therapy. *Cancer Treat. Rev.* **63**, 40–47 (2018).
28. M. Stoeckius, S. Zheng, B. Houck-Loomis, S. Hao, B. Z. Yeung, W. M. Mauck, P. Smibert, R. Satija, Cell hashing with barcoded antibodies enables multiplexing and doublet detection for single cell genomics. *Genome Biol.* **19**, 224 (2018).
29. L. Spinelli, S. Carpentier, F. Montanana Sanchis, M. Dalod, T.-P. V. Manh, BubbleGUM: Automatic extraction of phenotype molecular signatures and comprehensive visualization of multiple gene set enrichment analyses. *BMC Genomics* **16**, 814 (2015).
30. P. A. Szabo, H. M. Levitin, M. Miron, M. E. Snyder, T. Senda, J. Yuan, Y. L. Cheng, E. C. Bush, P. Dogra, P. Thapa, D. L. Farber, P. A. Sims, Single-cell transcriptomics of human T cells reveals tissue and activation signatures in health and disease. *Nat. Commun.* **10**, 4706 (2019).
31. L. Gabryšová, M. Alvarez-Martinez, R. Luisier, L. S. Cox, J. Sodenkamp, C. Hosking, D. Pérez-Mazliah, C. Whicher, Y. Kannan, K. Potempa, X. Wu, L. Bhaw, H. Wende, M. H. Sieweke, G. Elgar, M. Wilson, J. Briscoe, V. Metzis, J. Langhorne, N. M. Luscombe, A. O'Garra, c-Maf controls immune responses by regulating disease-specific gene networks and repressing IL-2 in $CD4^{+}$ T cells. *Nat. Immunol.* **19**, 497–507 (2018).
32. C. D. Slade, K. L. Reagin, H. G. Lakshmanan, K. D. Klonowski, W. T. Watford, Placenta-specific 8 limits IFNγ production by CD4 T cells in vitro and promotes establishment of influenza-specific CD8 T cells in vivo. *PLOS ONE* **15**, e0235706 (2020).
33. A. E. Lukacher, L. A. Morrison, V. L. Braciale, B. Malissen, T. J. Braciale, Expression of specific cytolytic activity by H-2I region-restricted, influenza virus-specific T lymphocyte clones. *J. Exp. Med.* **162**, 171–187 (1985).
34. J. J. Zaunders, W. B. Dyer, B. Wang, M. L. Munier, M. Miranda-Saksena, R. Newton, J. Moore, C. R. Mackay, D. A. Cooper, N. K. Saksena, A. D. Kelleher, Identification of circulating antigen-specific CD4+ T lymphocytes with a CCR5+, cytotoxic phenotype in an HIV-1 long-term nonprogressor and in CMV infection. *Blood* **103**, 2238–2247 (2004).
35. K. A. Stuller, E. Flaño, CD4 T cells mediate killing during persistent gammaherpesvirus 68 infection. *J. Virol.* **83**, 4700–4703 (2009).
36. R. Browaeys, W. Saelens, Y. Saeys, NicheNet: Modeling intercellular communication by linking ligands to target genes. *Nat. Methods* **17**, 159–162 (2020).

Downloaded from https://www.science.org at Universit Catholique de Louvain on November 04, 2026

37. P. J. Norris, H. F. Moffett, O. O. Yang, D. E. Kaufmann, M. J. Clark, M. M. Addo, E. S. Rosenberg, Beyond help: Direct effector functions of human immunodeficiency virus type 1-specific CD4$^+$ T cells. *J. Virol.* **78**, 8844–8851 (2004).
38. D. M. Brown, A. T. Lampe, A. M. Workman, The differentiation and protective function of cytolytic CD4 T cells in influenza infection. *Front. Immunol.* **7**, 93 (2016).
39. D. Y. Oh, S. S. Kwek, S. S. Raju, T. Li, E. McCarthy, E. Chow, D. Aran, A. Ilano, C. C. S. Pai, C. Rancan, K. Allaire, A. Burra, Y. Sun, M. H. Spitzer, S. Mangul, S. Porten, M. V. Meng, T. W. Friedlander, C. J. Ye, L. Fong, Intratumoral CD4$^+$ T cells mediate anti-tumor cytotoxicity in human bladder cancer. *Cell* **181**, 1612–1625.e13 (2018).
40. A. Cachot, M. Bilous, Y.-C. Liu, X. Li, M. Saillard, M. Cenerenti, G. A. Rockinger, T. Wyss, P. Guillaume, J. Schmidt, R. Genolet, G. Ercolano, M. P. Protti, W. Reith, K. Ioannidou, L. de Leval, J. A. Trapani, G. Coukos, A. Harari, D. E. Speiser, A. Mathis, D. Gfeller, H. Altug, P. Romero, C. Jandus, Tumor-specific cytolytic CD4 T cells mediate immunity against human cancer. *Sci. Adv.* **7**, eabe3348 (2021).
41. S. Verma, D. Weiskopf, A. Gupta, B. McDonald, B. Peters, A. Sette, C. A. Benedict, Cytomegalovirus-specific CD4 T cells are cytolytic and mediate vaccine protection. *J. Virol.* **90**, 650–658 (2016).
42. T. Maehara, N. Kaneko, C. A. Perugino, H. Mattoo, J. Kers, H. Allard-Chamard, V. S. Mahajan, H. Liu, S. J. H. Murphy, M. Ghebremichael, D. Fox, A. S. Payne, R. Lafyatis, J. H. Stone, D. Khanna, S. Pillai, Cytotoxic CD4$^+$ T lymphocytes may induce endothelial cell apoptosis in systemic sclerosis. *J. Clin. Invest.* **130**, 2451–2464 (2020).
43. J. A. Juno, D. van Bockel, S. J. Kent, A. D. Kelleher, J. J. Zaunders, C. M. L. Munier, Cytotoxic CD4 T cells—Friend or foe during viral infection? *Front. Immunol.* **8**, 19 (2017).
44. E. R. Jellison, S.-K. Kim, R. M. Welsh, Cutting edge: MHC class II-restricted killing in vivo during viral infection. *J. Immunol.* **174**, 614–618 (2005).
45. N. A. Scott, Y. Zhao, B. Krishnamurthy, S. I. Mannering, T. W. H. Kay, H. E. Thomas, IFNγ-induced MHC class II expression on islet endothelial cells is an early marker of insulitis but is not required for diabetogenic CD4$^+$ T cell migration. *Front. Immunol.* **9**, 2800 (2018).
46. J. E. Wosen, D. Mukhopadhyay, C. Macaubas, E. D. Mellins, Epithelial MHC class II expression and its role in antigen presentation in the gastrointestinal and respiratory tracts. *Front. Immunol.* **9**, 2144 (2018).
47. P. Smith, L. A. Jeffers, M. Koval, Measurement of lung vessel and epithelial permeability in vivo with evans blue. *Methods Mol. Biol.* **2367**, 137–148 (2021).
48. M. E. Keir, M. J. Butte, G. J. Freeman, A. H. Sharpe, PD-1 and its ligands in tolerance and immunity. *Annu. Rev. Immunol.* **26**, 677–704 (2008).
49. G. Schönrich, M. J. Raftery, The PD-1/PD-L1 axis and virus infections: A delicate balance. *Front. Cell. Infect. Microbiol.* **9**, 207 (2019).
50. H. W. Virgin, The virome in mammalian physiology and disease. *Cell* **157**, 142–150 (2014).
51. P. Brodin, V. Jojic, T. Gao, S. Bhattacharya, C. J. Angel, D. Furman, S. Shen-Orr, C. L. Dekker, G. E. Swan, A. J. Butte, H. T. Maecker, M. M. Davis, Variation in the human immune system is largely driven by non-heritable influences. *Cell* **160**, 37–47 (2015).
52. P. C. Doherty, J. P. Christensen, G. T. Belz, P. G. Stevenson, M. Y. Sangster, Dissecting the host response to a γ-herpesvirus. *Philos. Trans. R. Soc. B Biol. Sci.* **356**, 581–593 (2001).
53. P. G. Stevenson, Immune evasion by gamma-herpesviruses. *Curr. Opin. Immunol.* **16**, 456–462 (2004).
54. F. Saito, T. Ito, J. M. Connett, M. A. Schaller, W. F. Carson, C. M. Hogaboam, R. Rochford, S. L. Kunkel, MHV68 latency modulates the host immune response to influenza A virus. *Inflammation* **36**, 1295–1303 (2013).
55. A. Haque, N. Rachinel, M. R. Quddus, S. Haque, L. H. Kasper, E. Usherwood, Co-infection of malaria and γ-herpesvirus: Exacerbated lung inflammation or cross-protection depends on the stage of viral infection. *Clin. Exp. Immunol.* **138**, 396–404 (2004).
56. M. Dourcy, C. Maquet, L. Dams, G. Gilliaux, J. Javaux, D. Desmecht, M. Mack, B. G. Dewals, B. Machiels, L. Gillet, A gammaherpesvirus licenses CD8 T cells to protect the host from pneumovirus-induced immunopathologies. *Mucosal Immunol.* **13**, 799–813 (2020).
57. Y. Yao, M. Jeyanathan, S. Haddadi, N. G. Barra, M. Vaseghi-Shanjani, D. Damjanovic, R. Lai, S. Afkhami, Y. Chen, A. Dvorkin-Gheva, C. S. Robbins, J. D. Schertzer, Z. Xing, Induction of autonomous memory alveolar macrophages requires T cell help and is critical to trained immunity. *Cell* **175**, 1634–1650.e17 (2018).
58. D. Weiskopf, D. J. Bangs, J. Sidney, R. V. Kolla, A. D. de Silva, A. M. de Silva, S. Crotty, B. Peters, A. Sette, Dengue virus infection elicits highly polarized CX3CR1+ cytotoxic CD4+ T cells associated with protective immunity. *Proc. Natl. Acad. Sci. U.S.A.* **112**, E4256–E4263 (2015).
59. B. J. Meckiff, K. Ladell, J. E. McLaren, G. B. Ryan, A. M. Leese, E. A. James, D. A. Price, H. M. Long, Primary EBV infection induces an acute wave of activated antigen-specific cytotoxic CD4+ T cells. *J. Immunol.* **203**, 1276–1287 (2019).
60. L. M. Peeters, M. Vanheusden, V. Somers, B. van Wijmeersch, P. Stinissen, B. Broux, N. Hellings, Cytotoxic CD4+ T cells drive multiple sclerosis progression. *Front. Immunol.* **8**, 1160 (2017).
61. B. J. Meckiff, C. Ramírez-Suástegui, V. Fajardo, S. J. Chee, A. Kusnadi, H. Simon, S. Eschweiler, A. Grifoni, E. Pelosi, D. Weiskopf, A. Sette, F. Ay, G. Seumois, C. H. Ottensmeier, P. Vijayanand, Imbalance of regulatory and cytotoxic SARS-CoV-2-reactive CD4+ T cells in COVID-19. *Cell* **183**, 1340–1353.e16 (2020).
62. K. Hashimoto, T. Kouno, T. Ikawa, N. Hayatsu, Y. Miyajima, H. Yabukami, T. Terooatea, T. Sasaki, T. Suzuki, M. Valentine, G. Pascarella, Y. Okazaki, H. Suzuki, J. W. Shin, A. Minoda, I. Taniuchi, H. Okano, Y. Arai, N. Hirose, P. Carninci, Single-cell transcriptomics reveals expansion of cytotoxic CD4 T cells in supercentenarians. *Proc. Natl. Acad. Sci. U.S.A.* **116**, 24242–24251 (2019).
63. W. Ouyang, S. Rutz, N. K. Crellin, P. A. Valdez, S. G. Hymowitz, Regulation and functions of the IL-10 family of cytokines in inflammation and disease. *Annu. Rev. Immunol.* **29**, 71–109 (2011).
64. A. M. Siegel, J. H. Herskowitz, S. H. Speck, The MHV68 M2 protein drives IL-10 dependent B cell proliferation and differentiation. *PLOS Pathog.* **4**, e1000039 (2008).
65. K. W. Moore, P. Vieira, D. F. Fiorentino, M. L. Trounstine, T. A. Khan, T. R. Mosmann, Homology of cytokine synthesis inhibitory factor (IL-10) to the Epstein-Barr virus gene BCRFI. *Science* **248**, 1230–1234 (1990).
66. A. K. Kimball, L. M. Oko, R. E. Kaspar, L. F. van Dyk, E. T. Clambey, High-dimensional characterization of IL-10 production and IL-10–dependent regulation during primary gammaherpesvirus infection. *ImmunoHorizons* **3**, 94–109 (2019).
67. J. Sun, A. Cardani, A. K. Sharma, V. E. Laubach, R. S. Jack, W. Müller, T. J. Braciale, Autocrine regulation of pulmonary inflammation by effector T-cell derived IL-10 during infection with respiratory syncytial virus. *PLOS Pathog.* **7**, e1002173 (2011).
68. J. Attanasio, E. J. Wherry, Costimulatory and coinhibitory receptor pathways in infectious disease. *Immunity* **44**, 1052–1068 (2016).
69. M. J. Butte, M. E. Keir, T. B. Phamduy, A. H. Sharpe, G. J. Freeman, Programmed death-1 ligand 1 interacts specifically with the B7-1 costimulatory molecule to inhibit T cell responses. *Immunity* **27**, 111–122 (2007).
70. L. Wang, K. Pino-Lagos, V. C. De Vries, I. Guleria, M. H. Sayegh, R. J. Noelle, Programmed death 1 ligand signaling regulates the generation of adaptive Foxp3+CD4+ regulatory T cells. *Proc. Natl. Acad. Sci. U.S.A.* **105**, 9331–9336 (2008).
71. D. B. Johnson, J. M. Balko, M. L. Compton, S. Chalkias, J. Gorham, Y. Xu, M. Hicks, I. Puzanov, M. R. Alexander, T. L. Bloomer, J. R. Becker, D. A. Slosky, E. J. Phillips, M. A. Pilkinton, L. Craig-Owens, N. Kola, G. Plautz, D. S. Reshef, J. S. Deutsch, R. P. Deering, B. A. Olenchock, A. H. Lichtman, D. M. Roden, C. E. Seidman, I. J. Koralnik, J. G. Seidman, R. D. Hoffman, J. M. Taube, L. A. Diaz, R. A. Anders, J. A. Sosman, J. J. Moslehi, Fulminant myocarditis with combination immune checkpoint blockade. *N. Engl. J. Med.* **375**, 1749–1755 (2016).
72. R. A. Marsh, Epstein-Barr virus and hemophagocytic lymphohistiocytosis. *Front. Immunol.* **8**, 1902 (2018).
73. S. Grebinoski, A. M. Gocher-Demske, D. A. A. Vignali, Catch and release: Freeing up PD-L1 ameliorates autoimmunity. *Nat. Immunol.* **23**, 344–346 (2022).
74. D. Blaskovic, M. Stanceková, J. Svobodová, J. Mistríková, Isolation of five strains of herpesviruses from two species of free living small rodents. *Acta Virol.* **24**, 468 (1980).
75. R. Milho, C. M. Smith, S. Marques, M. Alenquer, J. S. May, L. Gillet, M. Gaspar, S. Efstathiou, J. P. Simas, P. G. Stevenson, In vivo imaging of murid herpesvirus-4 infection. *J. Gen. Virol.* **90**, 21–32 (2009).
76. Z. Gu, L. Gu, R. Eils, M. Schlesner, B. Brors, Circlize implements and enhances circular visualization in R. *Bioinformatics* **30**, 2811–2812 (2014).

Acknowledgments: We thank P. Fallon, B. Becher, C. Desmet, T. Marichal, and F. Bureau for providing mice and for helpful discussion. In particular, CD274^{tm1Pfal} mice were obtained [with material transfer agreement (MTA)] from P. Fallon (Trinity College Dublin) and Ccr2-creER^{T2} mKate2 mice were obtained (with MTA) from B. Becher (Institute of Experimental Immunology, Zurich University). We also thank C. Clercx and K.-T. Phan (Faculty of Veterinary Medicine, ULiège) for their valuable help in measuring the hematocrit parameter; staff members from the GIGA Mouse facility; C. Humblet from the GIGA Immunohistology Platform; L. Karim and members from the GIGA Genomics Platform; the NIH Tetramer Facility for the tetramers H-2D^b-ORF6$^{487–495}$ and H-2K^b-ORF61$^{521–531}$; B. G. Dewals and A. Vanderplasschen for insightful discussions; and the technician and administrative team of the Immunology-Vaccinology laboratory, especially L. Dams and C. Espert, for their very helpful assistance. **Funding:** This work was supported in part by the F.R.S./FNRS (research fellow for C.M., P.L., and L.R.-R.; research associate support for B.M.; F.R.S./FNRS "incentive grant for scientific research to B.M., 40003542"), in part by the ERC Starting Grant (to B.M.) (ERC-StG-2019 VIROME, ID:853608), in part by the grant from Leon Fredericq Foundation (to C.M.), and by the EOS joint programme of F.R.S./FNRS-FWO (EOS ID: 30981113) (to L.G.). **Author contributions:** C.M., L.G., and B.M. initiated the study and designed the experiments. J.J., R.S., P.L., L.R.-R., B.M., and C.M. did most of the experiments. C.M. compiled the data; J.B. performed the transcriptomic analyses and supervised the bioinformatic and statistical analyses; F.P. and D.C. prepared the slides for immunohistochemistry; M.M. provided the MC21-depleting antibody; P.G.F. provided the CD274^{tm1Pfal} mice; C.M., L.G., and B.M. analyzed the data; C.M. prepared the figures; L.R.-R.

Downloaded from https://www.science.org at Universit Catholique de Louvain on November 04, 2026

provided input for research design and interpretation and edited the manuscript; L.G. and B.M. wrote the manuscript and supervised the work. **Competing interests:** The authors declare that they have no competing interests. **Data and materials availability:** scRNA-seq data are deposited in GEO under accession number GSE205923 (NCBI tracking system #2304568). All data needed to evaluate the conclusions in the paper are present in the paper or the Supplementary Materials. List of mouse lines, reagents, and software used is provided in the Supplementary Materials and table S1. $CD274^{tm1Pfal}$ mice are available from P.G.F. under an MTA with the Trinity College Dublin, and $Ccr2\text{-}creER^{T2}$ mKate2 mice are available from B. Becher under an MTA with the Institute of Experimental Immunology, Zurich University.

Submitted 18 November 2021
Accepted 22 June 2022
Published 15 July 2022
10.1126/sciimmunol.abn3240

Downloaded from https://www.science.org at Universit Catholique de Louvain on November 04, 2026

Science Immunology

Ly6C^{hi} monocytes balance regulatory and cytotoxic CD4 T cell responses to control virus-induced immunopathology

Céline Maquet, Jérôme Baiwir, Pauline Loos, Lucia Rodriguez-Rodriguez, Justine Javaux, Rémy Sandor, Fabienne Perin, Padraic G. Fallon, Matthias Mack, Didier Cataldo, Laurent Gillet, and Bénédicte Machiels

Sci. Immunol. **7** (73), eabn3240. DOI: 10.1126/sciimmunol.abn3240

Monocyte mediator

Gammaherpesviruses (#HVs) coevolved with their hosts in a manner that allows for the lifelong persistence of these viruses in immunocompetent individuals. The presence of latent #HVs in host organisms has been shown to shape adaptive immunity, and here, Maquet *et al.* observed that pulmonary infection of mice with a murine #HV (MuHV-4) leads to recruitment of Ly6Chi monocytes (MOs) to airways. These #HV-imprinted Ly6Chi MOs recruit CD4 T cells to airways followed by engagement of the immunosuppressive PD-1/PD-L1 signaling pathway, which limits pathological cytotoxic CD4 T cell responses. These findings highlight a role for #HV-imprinted Ly6Chi MOs in shaping CD4 T cell functions and suggest a potential pathway for the development of therapeutics that target respiratory viral infections.

View the article online
https://www.science.org/doi/10.1126/sciimmunol.abn3240
Permissions
https://www.science.org/help/reprints-and-permissions

Downloaded from https://www.science.org at Universit Catholique de Louvain on November 04, 2026

Use of this article is subject to the Terms of service

Science Immunology (ISSN 2470-9468) is published by the American Association for the Advancement of Science. 1200 New York Avenue NW, Washington, DC 20005. The title *Science Immunology* is a registered trademark of AAAS.

Copyright © 2022 The Authors, some rights reserved; exclusive licensee American Association for the Advancement of Science. No claim to original U.S. Government Works